



HAL
open science

Mechanical and physical properties of inorganic polymer cement made of iron-rich laterite and lateritic clay: A comparative study

Cyriaque Rodrigue Kaze, Gisèle Laure Lecomte-Nana, Elie Kamseu, Paula Sanz Camacho, Antonia Yorkshire, John Provis, Mathieu Duttine, Alain Wattiaux, Uphie Chinje Melo

► To cite this version:

Cyriaque Rodrigue Kaze, Gisèle Laure Lecomte-Nana, Elie Kamseu, Paula Sanz Camacho, Antonia Yorkshire, et al.. Mechanical and physical properties of inorganic polymer cement made of iron-rich laterite and lateritic clay: A comparative study. *Cement and Concrete Research*, 2021, 140, 106320 (15 p.). 10.1016/j.cemconres.2020.106320 . hal-03053919

HAL Id: hal-03053919

<https://hal.science/hal-03053919v1>

Submitted on 15 Dec 2022

HAL is a multi-disciplinary open access archive for the deposit and dissemination of scientific research documents, whether they are published or not. The documents may come from teaching and research institutions in France or abroad, or from public or private research centers.

L'archive ouverte pluridisciplinaire **HAL**, est destinée au dépôt et à la diffusion de documents scientifiques de niveau recherche, publiés ou non, émanant des établissements d'enseignement et de recherche français ou étrangers, des laboratoires publics ou privés.



Distributed under a Creative Commons Attribution - NonCommercial 4.0 International License

Mechanical and physical properties of inorganic polymer cement made of iron-rich laterite and lateritic clay: A comparative study

Cyriaque Rodrigue Kaze^{1,2,*}, Gisèle Laure Lecomte-Nana^{2,**}, Elie Kamseu³, Paula Sanz Camacho⁴, **Antonia S. Yorkshire**⁵, John L. Provis⁵, Mathieu Duttine⁴, Alain Wattiaux⁴, Uphie Chinje Melo¹

¹ Laboratory of applied inorganic chemistry, Faculty of science, University Yaoundé I, BP 812 Yaoundé, Cameroon.

² CNRS, ENSIL-ENSCI, University of Limoges, CEC, IRCER UMR 7315, 87068 Limoges, France.

³ Laboratory of materials, Local Materials Promotion Authority, MINRESI/MIPROMALO, P.O. Box 2396, Yaoundé, Cameroon

⁴ CNRS, Univ. Bordeaux, Bordeaux INP, ICMCB UMR 5026, F-33600 Pessac, France.

⁵ Department of Materials Science and Engineering, The University of Sheffield, Sir Robert Hadfield Building, Sheffield S1 3JD, UK.

*Corresponding author: kazerodrigue@gmail.com (R. C. Kaze)

**Corresponding author. Tel.: +33 587 50 25 59; fax: +33 587 50 23 01. E-mail address: gisele.lecomte@unilim.fr (G. Lecomte-Nana)

Abstract

In this work, two different laterites (iron contents of 13.07 and 49.34 wt%, respectively, for lateritic clay, LAC, and iron-rich laterite, LAI) were selected and calcined at 600 °C. The obtained calcined laterites, namely LAI600 and LAC600, were separately mixed with an alkaline solution (silicate modulus of 1.35) or an acidic solution (phosphoric acid solution at $\text{pH} \leq 2$) for the synthesis of inorganic polymer products. The fabricated products were cured at 20 °C (ambient) and 40 °C (oven). The obtained results showed that the compressive strength of each series of alkaline-based inorganic polymer binder increased with ageing time (7 and 28 days) for room temperature curing, while the reverse trend was noted for oven-cured specimens. The best mechanical performance was obtained when using a phosphoric acid solution, 38 and 52 ± 1 MPa; 62 and 65 ± 1 MPa at 28 days for LAC and LAI respectively. It appeared that a higher iron content within the laterite contributed to an increase in the compressive strength under acidic conditions (LAI (59 MPa) > LAC (48 MPa)) compared to the behaviour obtained under alkaline conditions (LAI (6 MPa) < LAC (29 MPa)). Accordingly, the acidic products

exhibited a dense structure (with lower porosity) and contained amorphous iron/aluminium phosphate phases such as berlinite (FePO_4), iron hydrogen phosphate hydrate ($\text{Fe}_3\text{H}_{15}(\text{PO}_4)_8 \cdot 4\text{H}_2\text{O}$), ferrowyllieite ($\text{AlFe}_2\text{Na}_2(\text{PO}_4)_3$) and sodium iron phosphate ($\text{Na}_3\text{Fe}_2(\text{PO}_4)_3$) arising from the alteration of iron minerals in an acidic medium, confirmed by Mössbauer spectroscopy and electron paramagnetic resonance spectroscopy.

Keywords: Laterite, sodium silicate, phosphoric acid, inorganic polymer cement, mechanical properties, electron paramagnetic resonance, ^{57}Fe Mössbauer spectroscopy

1. Introduction

Laterites and lateritic clays are typically formed from the alteration of kaolinite by iron mineral phases such as goethite ($\alpha\text{-FeO(OH)}$), lepidocrocite ($\gamma\text{-FeO(OH)}$) and hematite (Fe_2O_3) where a high proportion of aluminium (Al^{3+}), occupying octahedral sites, is substituted by iron (Fe^{3+} and Fe^{2+}) [1, 2]. This alteration is referred to in the literature as induration or laterisation, resulting from sedimentation or leaching processes, under the combined actions of humidity and temperature gradients [3]. Lateritic soils are generally composed of iron, silicon and aluminium oxides [4-7]. In the last few years, these soils, containing iron minerals, have been considered as solid precursors for alkali-activated materials. Alkali-activated binders, including those sometimes described as geopolymers, are materials formed by the mixing of aluminosilicate powders with alkaline solution at a temperatures less than 100°C , through the geopolymerisation process [8] or dissolution and precipitation mechanisms. Binders produced by acid-phosphate activation of aluminosilicate powders are also described by some researchers as geopolymers” due to analogies between alkali-activation and acid-activation chemistry [9].

The common solid precursors generally used for geopolymer syntheses are metakaolin obtained by calcining kaolin clays [10-14], industrial wastes or by-products such as slag and fly ashes, [15-17] and volcanic ashes [18, 19]. The geopolymer products can have diverse characteristics such as good thermo-mechanical properties [19, 20], lower CO_2 emissions than Portland cement [21], and good durability in acidic or salt solutions [12, 22, 23]. Based on these aforementioned attractive characteristics, alkali-activated binders appear as a good alternative solution to Portland cement in suitable applications, and where appropriate raw materials are available for their production. It is well known that the final properties of these binders can be affected by the chemical compositions of the reagents, the chemical and mineralogical composition of solid precursors used, and the curing conditions adopted (temperature and relative humidity) [6, 18, 23, 24]. Focusing on the work reported thus far [2, 4, 6, 7, 25-31], the

properties of alkali-activated matrices produced from lateritic materials are satisfactory, but vary depending on the synthesis conditions. Taking into account the mechanical performance of alkali activated materials formulated using laterite, and its widespread availability as a geological resource, there is potential for its use as a solid precursor to substitute commonly used aluminosilicates [25, 27, 31].

Lecomte et al. [2] reported on laterite-based geomaterials that were oven-cured at 60 °C, reaching a compressive strength between 12 and 20 MPa, formulated from mixture of laterite clay (55.2 wt.% kaolinite) with nitric acid/calcium hydroxide and fulvic acid/calcium hydroxide, respectively. Goure-Doubi et al. [4] investigated the mechanical and thermal properties of raw laterite activated with fulvic acid, using lime or sodium hydroxide for neutralization, before curing at 60 °C in an oven for 18 days, recording strengths approaching 1 MPa in both cases. They concluded that the latter product was less stable when immersed in water, as the cementitious phases formed through lime addition were beneficial for durability. The findings of Kaze et al. [26, 28] and Bewa et al. [24], using an alkaline silicate solution and phosphoric acid, respectively, as activators for the synthesis of iron-rich laterite-based geopolymers, gave reasonable properties depending on the synthesis conditions and mineralogical composition. The structural and microstructural properties of laterite-based inorganic polymer binders, using raw or calcined laterites activated with different chemical reagents, have also been explored for building applications. Lecomte-nana et al. [30] showed that the dissolution of iron minerals from raw laterite in fulvic acid led to the development of a hydrated iron-rich binder phase, contributing to the strength development of the material. Although some studies have investigated the role of Fe in both clay-based [32, 33] and red mud-based binders [34] the behavior of iron minerals in these binder phases, and the role of iron throughout the reaction processes, has not yet been investigated in detail for alkali- and acidic-activated materials.

It is clear that as a result of their availability around the world, laterites appear as a good candidate for production of alkali- or acid-activated inorganic polymer binders. In this present study, we have therefore analyzed the effect of chemical treatments (acidic and alkaline) on the geopolymerization of lateritic materials. The suitability of two different lateritic materials from Cameroon, calcined at 600 °C, for the fabrication of inorganic polymer (geopolymer) cements as construction materials, was investigated. Structural and microstructural analysis of the hardened geopolymers was conducted by means of X-ray diffraction (XRD), Fourier transform infrared spectroscopy (FTIR) and scanning electron microscopy (SEM). From these results, it

was determined that the acidic or alkaline consolidation of lateritic soils is controlled by the physicochemical and mineralogical composition, which may affect their reactivity and end performances of the cured product. Further characterizations of the obtained inorganic polymer binders highlighted a possible correlation between the consolidation medium of the laterites (acidic or alkaline) and their final properties, such as compressive strength and thermal conductivity. Further to this, the assemblage of iron minerals from both laterites was assessed using ^{57}Fe Mössbauer spectroscopy and Electron resonance paramagnetic (EPR) spectroscopy.

2. Experimental procedures

2.1 Materials

Iron-rich laterite and lateritic clay used in the present work were collected in Montée des Soeurs (3° 50' 25" North, 11° 29' 12" East) and Ngoa-Ekelle (clay deposit, 3° 52' 0" North, 11° 31' 58" East) in Yaoundé town, Cameroon. The raw materials were dried and ground to reach a particle size of under 80 μm . The resulting powders were labelled LAI (iron-rich laterite from Montée des Soeurs) and LAC (lateritic clay from Ngoa-Ekelle). The powders were heated at 600 °C for 4h (heating/cooling rate of 5 °C/min) in a programmable electrical furnace and are hereafter denoted LAI600 and LAC600. This temperature profile was used according to previous work [26]. The particle size distributions of the laterites were determined with a Mastersizer 2000 Ver. 5.22 (Malvern Instruments Ltd.), indicating average particle sizes, d_{50} , of 18.1 and 40.2 μm respectively, for the calcined lateritic clay (LAC600) and iron-rich laterite (LAI600).

2.2 Geopolymer preparation

For the synthesis of inorganic polymer binders, both calcined laterites were mixed separately with each activating solution (sodium silicate or phosphoric acid). The liquid/solid mass ratios were 0.6 and 0.8, respectively, for calcined iron-rich laterite (LAI600) and calcined lateritic clay (LAC600), to enable sufficient workability of both pastes. The fresh pastes were cast into cylindrical moulds with dimensions of 30 mm (diameter) x 60 mm (height). One group of samples was kept at room temperature (20 ± 3 °C), and a second group was oven cured at 40 °C for 24 h before demoulding. The majority of samples were observed to set within reasonable timeframes: 3-4 hours for the alkali-activated samples at room temperature, and all of the oven-

cured samples hardened in time for demoulding. The room-temperature acid-activated samples were somewhat slower to set, taking 3-4 days. The cylindrical specimens were labelled LACAS and LAIAS when consolidated with an alkaline solution (AS); LACPA and LAIPA when consolidated with phosphoric acid (PA). The process is described and summarised in Figure 1.

The alkaline activator solution used was obtained by mixing sodium silicate solution (8.0 wt.% Na₂O, 26.2 wt.% SiO₂, 65.8 wt.% H₂O; supplied by Prolabo Chemicals, France) and 10 mol/L aqueous NaOH solution at a mass ratio sodium silicate/sodium hydroxide = 2. Phosphoric acid solution of concentration 10 mol/L was obtained by dilution of commercial aqueous phosphoric acid (H₃PO₄, 85% w/w_{aq} supplied by Alfa Aesar, France) in deionised water.

2.3 Characterisation methods

2.3.1 Phase analysis

The chemical composition of both raw and calcined laterites was determined using X-ray fluorescence spectroscopy (Bruker S8 Tiger). Before analysis, each powder sample was mixed with lithium borate and vitrified within a Pt crucible at 1060 °C. The loss on ignition at 1050 °C was also measured to calculate the final chemical compositions.

X-ray diffraction was performed with a reflection Bruker-AXS D8 Advance Debye-Scherrer diffractometer using Cu K α radiation ($\lambda = 1.54056 \text{ \AA}$) and a graphite monochromator. The analysis range was between 5 and 70° 2 θ with a step-size of 0.04° and an acquisition time of 2s/step. The crystalline phases present were identified by comparison with ICDD (International Centre for Diffraction Data) PDF (Powder Diffraction Files) records.

Infrared spectroscopy measurements were performed on a Thermo Fisher Scientific Nicolet 380 instrument in transmission mode, operating in attenuated total reflectance (ATR) mode using a diamond crystal. For the measurement's powders of each sample (raw and calcined laterites, and geopolymer products) were used; FTIR spectra were recorded over the range 4000 to 400 cm⁻¹ at a resolution of 4 cm⁻¹ with 64 scans.

2.3.2 DTA/TG analysis

Differential thermal analysis (DTA), coupled with thermogravimetric analysis (TGA), was performed on a Labsys Evo instrument (DTA-TGA equipment from SETARAM). The analyses were carried out under air, from ambient temperature to 1200 °C. A quantity of 100 mg of

powder was placed in a Pt crucible with two heating ramps of 5 and 20 °C /min under air flow. The sample and the reference were placed in two identical Pt crucibles.

2.3.3 Mechanical properties

The mechanical performance of hardened specimens was determined using an Instron 6959 instrument with a constant displacement rate of 0.5 mm/min. The values reported are averaged over five replicate specimens, with an associated standard deviation of ± 1 MPa within each set of replicates.

The thermal conductivity measurements of the inorganic polymer binders were characterised using a transient plane source (TPS) technique operating at room temperature, supplied by Hot Disk AB (Sweden). The measurements of each formulation were assessed following the procedure described by Bourret et al. [35].

The water absorption, total porosity and apparent density were evaluated by the Archimedes method using an electric balance (Sartorius model 1712001) with a sensitivity of ± 0.001 g. Before weighing, the specimens were dried in an oven at 40 °C until they reached a constant mass.

2.3.4 Microstructural analysis

Specimens obtained from the samples used in mechanical testing were analysed using a JEOL IT300LV scanning electron microscope (SEM) coupled with EDS, with an acceleration voltage of 40.0 kV. The samples were coated with a thin Pt layer to improve their surface conductivity.

2.3.5 ^{57}Fe Mössbauer spectroscopy

To facilitate better understanding of iron mineral phases after acidic and alkaline treatment and their influence on the structural and microstructural evolution of hardened products, ^{57}Fe Mössbauer spectroscopy was performed on eight series of lateritic samples: LAC, LAC600, LACAS, LAIPA, LAI, LAI600, LAIAS and LAIPA. The samples were analysed in transmission mode using a HALDER spectrometer with a constant acceleration using a ^{57}Co source (rhodium matrix) at room temperature (293K). Sample suspensions were prepared from finely ground powders placed in waterproof nylon sample holders. The analysed aliquots were optimised so that the iron surface concentration was approximately 10 mg/cm². At these

concentrations, saturation phenomena leading to a widening of the lines can be neglected. The spectral calculation was performed in two steps using two computational programs. The first calculation method allowed the spectra to be calibrated using Lorentzian profile lines. The position, amplitude and width of each line were refined. This approach provides a first estimate of the experimental hyperfine parameters of the different iron sites. The second method of calculation allowed processing of the spectra to obtain a distribution of hyperfine parameters $P(\Delta)$ and/or $P(\text{Bhf})$ using the method of Hesse and Rubartsch [36]. This method is often used for disordered compounds, for which there is a wide distribution of possible environments that result in large width spectral lines, and whose shape may deviate from a Lorentzian profile. For this calculation, the line width was set at half height (Γ) at a value of $0.25 \text{ mm}\cdot\text{s}^{-1}$. The isomeric displacements (δ) and, in the case of sextuplets, the quadrupolar displacements (ϵ) used were those deduced from the first calculation method. From the experimental spectrum, a quadrupolar burst distribution, $P(\Delta)$ (or "P(Qua)"), or a hyperfine field distribution, $P(\text{Bhf})$, was then extracted for each iron species to calculate average parameters of Δ (or "Qua") or Bhf . The relative percentages were refined for each distribution studied. Isomeric displacements were reported relative to α -iron at 293 K.

2.3.6 Electron paramagnetic resonance (EPR) spectroscopy

The EPR spectra of the inorganic polymer cements were recorded on a Bruker ESP300E spectrometer at 9.54 GHz (X-band) microwave frequency. The EPR spectra of the starting materials (LAC, LAC600, LAI and LAI600) and synthesised inorganic polymer binders (LACAS, LACPA, LAIAS and LAIPA) were recorded at 293 K using a cooled nitrogen flow device. The investigational parameters were as follows: 10 mW microwave power and 100 kHz frequency modulation of the magnetic field; 1 mT modulation amplitude of the magnetic field. The spectra were recorded in the magnetic field range of 0-675 mT, with a spectral resolution of 0.6 mT/point and measurement time of 82 ms/point. The magnetic field was applied with DPPH ($g = 2.0036 \pm 0.0002$) used as a reference.

3. Results and discussion

3.1 Characterisation of Iron-rich laterite and lateritic clay

3.1.1 Chemical and mineralogical composition

Both laterites studied were mainly composed of Fe_2O_3 , SiO_2 and Al_2O_3 as major oxides (Table 1). The higher iron content observed in the iron-rich laterite (almost 50 wt.%) is indicated by its red-brown colour and explains the presence of the iron-rich minerals goethite (α -

FeO(OH)), hematite (α -Fe₂O₃) and ilmenite (FeTiO₃) as confirmed by XRD analysis (Figure 2). In the raw laterites, the Si/Al ratios were 1.16 and 1.53, respectively, for LAI and LAC. The Si/Al ratio in the LAI sample is similar to that of standard kaolin clay, while the higher ratio for LAC could be due to the presence of a second (possibly 2:1) clay mineral, such as illite, or a high content of amorphous silica and quartz. Al in the clay minerals is also likely to be partially substituted by Fe; this substitution tends to induce some structural disorder, leading to a reduction in crystallinity [22, 26], showing that their use as a solid precursor for the formation of binders may be possible with lower energy for thermal activation than is the case for more ordered clays, making this process more environmentally attractive compared to calcination of purer kaolin. Further to this, the kaolinite content was higher in the lateritic clay (54.2 %) than in the iron-rich laterite (38.2 %). These values were calculated using TG/DTA curves recorded for each sample. The difference in kaolinite content in both the raw laterites used justifies the chosen alkaline solution/calcined laterite ratios (i.e., mass ratios of 0.6 and 0.8 respectively), to allow for acceptable workability during the synthesis of the geopolymer binders. The higher liquid/solid ratio of 0.8 used in the geopolymer binder formed from 600 °C calcined lateritic clay is related to the high content of kaolinite (in LAC) which was transformed completely into metakaolin. The high metakaolin content in the calcined lateritic clay (LAC600), and smaller particle size (see section 2.1), requires a higher volume of liquid to account for its high water demand, compared to the calcined iron-rich laterite (LAI600).

The X-ray diffraction patterns of both raw and calcined laterites are plotted in Figures 2a and 2b. The main mineral phases of raw laterites are goethite (α -FeO(OH), PDF# 00-046-1045), kaolinite (Al₂Si₂O₅(OH)₄, PDF# 01-083-4643), quartz (SiO₂, PDF# 00-046-1045), hematite (α -Fe₂O₃, PDF # 04-003-2900), ilmenite (FeTiO₃, PDF# 04-015-9381), maghemite (γ -Fe₂O₃, PDF# 01-084-1595), illite ((K,H₃O)(Al,Mg,Fe)₂(Si,Al)₄O₁₀[(OH)₂,(H₂O)]), PDF# 04-017-0523), iron aluminium oxyhydroxide (Fe_{0.93}Al_{0.07})O(OH), PDF# 00-059-0344) and anatase (TiO₂, PDF# 00-021-1272). However, the disappearance of kaolinite due to thermal treatment at 600 °C was observed in the diffractograms of both calcined laterites. This change is likely linked to the transformation of kaolinite into mekaolinite that occurred during calcination. The fact that the transformation is effective at 600 °C is linked to the alteration of kaolinite by iron substitution, which affects its crystalline structure [37] and reduces the temperature of dehydroxylation [38].

It should also be noted that this transformation induces the formation of a diffuse scattering feature in the diffractograms, situated between 15° and 35° 2 θ , highlighting the

formation of a glass-like or amorphous phase (Figure 2). The thermal analyses of lateritic clay and iron-rich laterite, presented in Figures 3a and 3b, respectively, allude to the physicochemical transformations that are occurring. Initially, endothermic peaks around 262 and 323 °C (Figures 3a and 3b) with a sharp decrease in weight (~1% in Figure 3b and ~6% in Figure 3a) are observed. This decrease was attributed to the dehydroxylation of goethite, described by Equation 1:



The second peak that appears in the TG/DTA thermograms at around 500 °C (Figures 3a and 3b), is linked to the transformation and dehydroxylation of kaolinite, via the loss of water from the kaolinite and resulting disruption to its layered structure [39], into disordered metakaolinite. This peak is more pronounced in the thermogram measured for the lateritic clay, with a weight loss of ~8%, indicating that this laterite contains more kaolinite compared to the iron-rich laterite, which exhibited only a 2.5% weight loss. Based on thermal analysis it can be concluded that the desired calcination temperature of these lateritic materials is between 500 and 600 °C. The exothermic peaks that occur at 958 and 982 °C are linked to the formation of mullite due to the structural reorganisation of metakaolinite, also influenced by the presence of iron-containing phases [40].

The infrared spectra of the raw and calcined laterites are plotted in Figures 4a and 4b. The absorption bands positioned at 3619, 3683 and 3688 cm⁻¹ were assigned to O-H and Al-OH stretching bonds of the kaolinite, in both LAI and LAC. However, these bands did not appear on the infrared spectra for both the calcined laterites (LAI600 and LAC600), as expected, indicating the complete dehydroxylation of kaolinite into metakaolinite. The absorption bands at 1001, 1110, 1128 cm⁻¹ are attributed to Si-O-Si and Fe(Al)-O-Si stretching modes [6, 10, 13] and those located at 904, 906 and 995 cm⁻¹ correspond to vibrational modes of Al-O-Si bonds. The low intensity bands at 784 and 798 cm⁻¹ were ascribed to the Si-O-Al(IV) bending vibrational mode [12, 13, 41] and those at 449, 528 and 528 cm⁻¹ were linked to the stretching modes of Fe-O, Si-O and Si-O-Al(IV) [2, 6, 24-26, 28, 30, 31].

3.2 Characterisation of consolidated inorganic polymer products

3.2.1 Phase evolution

The X-ray patterns of LAI600 and LAC600, and those of the hardened inorganic polymer binders obtained using phosphoric acid and alkaline solutions, are presented in Figures 5a and

5b respectively. In both calcined laterites, the **diffuse scattering** feature initially appearing between 15 and 25° 2 θ was shifted to appear between ~20-40° 2 θ after alkaline or acidic consolidation. This change is likely to be related to reactions between the calcined laterites and phosphoric acid or alkaline solutions leading to the formation of amorphous phases. Crystalline mineral phases **such as** hematite, quartz, ilmenite and anatase contained in the calcined laterites also **remain** after alkaline or acid consolidation; they are either unaffected or partially dissolved in the **acidic** or alkaline activating solutions. **Newly** formed mineral phases were identified by XRD, including fayalite (Fe₂SiO₄, PDF# 34-178), and a number of phosphates resulting from acid activation: iron hydrogen phosphate hydrate (Fe₃H₁₅(PO₄)₈·4H₂O, PDF# 00-045-0502), berlinite (FePO₄, PDF# 00-010-0423), ferrowyllieite (AlFe₂Na₂(PO₄)₃, PDF# 00-051-0508) and iron phosphate hydroxide (Fe₄(PO₄)₃(OH)₃, PDF# 00-047-0413).

Figures 6a and 6b display the infrared spectra of **the** inorganic polymer binders made from calcined lateritic clay and iron-rich laterite, **respectively**, consolidated with phosphoric acid and alkaline solutions. The bands located in all **the** infrared spectra of **the** laterite based inorganic polymer binders, between 419 and 441 cm⁻¹, are related to stretching of Si-O and Fe-O bonds, and the bands appearing at 530, 534, 538, 541 and 543 cm⁻¹ **were assigned to the vibrational mode** of Si-O-Al(VI). The broad bands at 1055 and 1057 cm⁻¹ exhibited **in the spectra** of both calcined iron-rich laterite and lateritic clay are shifted to lower (981 and 972 cm⁻¹) values **after activation with the** alkaline sodium silicate solution, suggesting the formation of newly formed phases (**which are, according to the XRD results and consistent with the literature for alkali-activation, likely to be disordered**), whereas **for** binders obtained from phosphoric acid **activation** these bands **are** shifted to higher wavenumbers 1070 and 1074 cm⁻¹, as indicated in Figure 4. This displacement might be linked to **either** the substitution of Al³⁺ by Fe³⁺, formation of phosphate-containing minerals as identified by XRD, or **the** possible insertion of [PO₄³⁻] units into tetrahedral **sites of the** inorganic polymer 3D network structure, either in silicophosphate or silico-aluminophosphate forms [42-45].

To **further corroborate** the occurrence of **new** hydrated and hydroxylated phases, the thermal analyses performed on the various inorganic polymer binders **were also considered**. Figures 7a and 7b **display** the DTA and TG curves of **the** consolidated inorganic polymer cements. There is **an** apparent thermal stability for the alkaline activated laterites, with only a small peak **related to** dehydroxylation at ~195 °C, **followed by** continued densification up to high temperature (850 °C). Acid activation resulted in **an** inorganic polymer cement that **presented** slight dehydration between 140 and 180 °C. The **small** endothermic peaks at around 200 °C resulting **from a small**

weight loss ($\leq 2\%$) for both samples consolidated with the alkaline solution are due to the loss of water content from the binder phase [46]. The weight loss ($\sim 4\%$) at $174\text{ }^{\circ}\text{C}$, for both samples consolidated with phosphoric acid, is assigned to the removal of chemically bonded water from amorphous iron hydrogen phosphate hydrate ($\text{Fe}_3\text{H}_{15}(\text{PO}_4)_8 \cdot 4\text{H}_2\text{O}$) and iron phosphate hydroxide ($\text{Fe}_4(\text{PO}_4)_3(\text{OH})_3$), or amorphous ferri- or ferro-phosphate binder phases [9, 47]. Finally, the exothermic peak situated between 842 and $853\text{ }^{\circ}\text{C}$ in the DTA data, without a notable mass loss in the TG curves, is likely related to the transformation of an amorphous ferriphosphate phase into trigonal ($\alpha\text{-FePO}_4$) and/or tetragonal ($\beta\text{-FePO}_4$) berlinite [45]. The last small peak around $955\text{-}963\text{ }^{\circ}\text{C}$ might be linked to the formation of mullite from residual metakaolinite, arising from both calcined laterites, which was not consumed during the alkaline reaction.

3.2.2 Mechanical and thermal properties of inorganic polymer cements

The measurements of 7- and 28-days compressive strength of laterite based inorganic polymer cements consolidated with alkaline solution (AS) and with phosphoric acid (PA) solution, cured at 20 and $40\text{ }^{\circ}\text{C}$, are reported in Table 2. In all formulations the compressive strength increased from 7 to 28 days: from 6 to 17 MPa and from 29 to 40 MPa for LAIAS and LACAS, respectively, when cured at room temperature ($20\text{ }^{\circ}\text{C}$). However, the reverse effect was observed for the corresponding oven-cured specimens ($40\text{ }^{\circ}\text{C}$ for 24 h), with a decrease in the compressive strength from 15 to 10 MPa and from 38 to 30 MPa , respectively, for LAIAS and LACAS. The high mechanical strength gained in the LACAS sample, compared to that of LAIAS, could be due to the high content of metakaolinite in the initial LAC compared to LAI, providing a reactive aluminosilicate to contribute to binder formation. The development of lower strength in the LAIAS sample might be due to the precipitation of iron with hydroxide ions, consuming the alkaline activator and preventing extension of binder phase formation that is responsible for the development of strength. The decrease in mechanical strength due to oven-curing could be explained by the earlier release of water from the matrix of the laterite-based inorganic polymer binder phase, promoting the development of cracks or pores, thus resulting in lower strength. This suggests that oven curing at $40\text{ }^{\circ}\text{C}$ should be avoided for laterite based inorganic polymer synthesis by alkaline activation, or applied only with controlled relative humidity.

The increase of curing temperature from 20 to $40\text{ }^{\circ}\text{C}$ for acidic activation favoured the increase of mechanical strength in samples based on both laterites (LAC600 and LAI600). The

compressive strengths increased from 7 to 28 days: from 48 to 52 MPa and 59 to 65 MPa, respectively, for LACPA and LAIPA samples. The highest strength achieved in the LAIPA sample is linked to the release of iron ions from the dissolution of iron mineral phases in the acidic medium, allowing the formation of amorphous iron-containing phases (observed in Mössbauer spectra, see below) such as berlinite, resulting in an increased extension of the inorganic polymer network. This could be responsible for the increased strength development of this sample. These results also evidence the potential reaction of iron minerals in acidic solution, despite their long setting time observed at room temperature during the synthesis of the resulting products. This parameter has not taken into account in the present work.

The values of the thermal conductivity of laterite based inorganic polymer cements are reported in Table 3. The acid-activated laterite based inorganic polymer, LAIPA, possesses higher values of thermal conductivity than the LACPA cements (see Table 3). This trend could be due to the iron content and the apparent density of structure within LAIPA samples, which will be explored in more detail below. The increase in thermal conductivity with curing time may be due to the increase in binding of water into hydrous reaction products. When both calcined laterites were consolidated using the alkaline solution, a similar trend was observed. These low values for oven cured samples, compared to those obtained for acidic activation, are in agreement with the lower strength development, suggesting the presence of cracks, pores and/or voids between the binder phase and other particles, which could result from incomplete binder phase formation. The microstructures of the samples will be explored in more detail in section 3.2.3.

The measurements of bulk density, water absorption and porosity are also reported in Table 3. The apparent density values ranged from 2.55 to 2.64 g·cm⁻³ and 2.7 to 2.77 g·cm⁻³ for the LAI specimens, and 2.02 to 2.20 g·cm⁻³ and 2.31 to 2.32 g·cm⁻³ for the LAC specimens, when consolidated with phosphoric acid and sodium silicate solution, respectively. The LAI samples generally displayed a higher apparent density than the LAC samples, which is related to the significantly lower water content of the LAI mixes (liquid/solids ratio of 0.6, compared to 0.8 for LAC mixes), and potentially also linked to the higher iron oxide content contributing to increased unit weight. The use of an alkaline activating solution also resulted in an increased apparent density, relative to the use of an acidic activating solution, for both the LAI and LAC samples, indicating some binding of water into the reaction products of alkali-activation. The curing temperature did not appear to exhibit any particular trend in terms of its effect on the measured values of the apparent density.

The values of water absorption (WA) and open porosity (OP) are also reported in Table 3. The low values of open porosity and water absorption obtained for the LAIPA and LACPA samples indicate their compact and dense nature, given their low water retention during water immersion. Conversely, the LAIAS and LACAS samples are hypothesised to display a large volume of nano- and micro-porosity that contribute to high water retention, and a higher volume of unreacted particles. The trend of the porosity results corroborates those of apparent density and compressive strength.

3.2.3 Microstructure

The fracture surfaces (at different magnifications) of the inorganic polymer binders are presented in Figures 8a and 8b, respectively, after 28 days of curing. It was observed that the matrix of the LAIAS sample (Figure 8a) appeared more heterogeneous with loosely packed 'globular' particles compared to LACAS (Figure 8b), which appeared more 'flaky' in nature. In the same micrographs it was observed that there were some grains or misshaped particles with a layered structure as well as micro-fissures and pores (Figure 8a). These observations match well with the mechanical strength results and might be due to the precipitation of iron hydroxide [48], which does not allow for effective polycondensation of binding phases in a way that would fill the microstructure with a dense gel. The LACAS sample possesses a more homogeneous and compact structure (Figure 8b), likely due to the high dissolution of metakaolin from its precursor powder, which allows greater extension of the binder phase within the laterite based inorganic polymer matrix, resulting in a more rigid structure. However, when phosphoric acid activation was used, both specimens LAIPA and LACPA exhibited a homogeneous structure that was compact and dense compared to the LAIAS and LACAS samples. In the higher resolution images within Figure 8, the binder phase responsible for the highest strength achieved in these samples (LACPA and LAIPA) can be described as being nanoparticulate (≤ 500 nm, Figure 8d) and dispersed across the matrix, forming a rigid block structure. The high extension of the binder phase in LACPA and LAIPA is in line with the highest strength gained by these samples. Therefore, the dissolution of iron minerals in an acidic medium allowed the formation of iron mineral phases (FePO_4 , $\text{AlFe}_2\text{Na}_2(\text{PO}_4)_3$, $\text{Na}_3\text{Fe}_2(\text{PO}_4)_3$, and $\text{Fe}_4(\text{PO}_4)_3(\text{OH})_3$ as indicated on XRD patterns, and which will be confirmed by the EPR spectra and Mössbauer spectroscopy results presented below. These phases have contributed to the densification of the inorganic polymers. For the samples LAIAS and LACAS oven cured at 40 °C (Figure 8c), the micrographs exhibit high porosity and cracking, which justify the lower values of compressive strength and apparent density, and high values of porosity obtained for

these samples. This explains why the oven cured alkali-activated samples did not show improved compressive strength (Table 2), whereas oven curing of LAIPA and LACPA specimens improved the compressive strength (Table 2). This could be related to a higher degree of dissolution for both calcined laterites in the acidic medium, favouring the formation of a binder phase by improving the connectivity/cohesion, thus resulting in higher compressive strength. From the qualitative EDS analysis (Figure 8d) the main atoms within the matrix are Na, Al, O, P, Fe and Si, indicating inclusion or close intermixing of iron into the silico-aluminate (in alkali-activated samples) and silico-aluminophosphate (in acid-activated samples) binding phases. This indicates the possible incorporation of iron, resulting from the dissolution of iron-rich minerals in the laterites, within the main binder phase [29, 45].

3.2.4 ⁵⁷Fe Mössbauer spectroscopy

3.2.4.1 Mössbauer spectra of LAC, LAC600, LACAS and LACPA samples

Figure 9a shows the Mössbauer spectra of unheated clay-rich laterite (LAC), the corresponding calcined laterites (LAC600) and the resulting inorganic polymer binders, LACAS and LACPA consolidated with alkaline (AS) solution and phosphoric acid (PA). The fitting results are presented in Table 4. For LAC, the experimental spectrum consists of two components: a majority component represented by a quadrupole splitting (Dis.2), and a magnetically ordered minority component, represented by a sextuplet distribution (Dis.1). The refinement of the spectrum leads to isometric displacement values that confirm that the two components are related to trivalent, high-spin iron. The hyperfine parameters of the minority component ($\delta = 0.36$ mm/s, $\varepsilon = -0.10$ mm/s and $B_{\text{hf}}^{\text{max}} = 50$ T) are very similar to those of hematite ($\delta = 0.7$ mm/s, $\varepsilon = -0.10$ mm/s and $B_{\text{hf}} = 51.5$ T) (Table 4). However, the very large dispersion of the distribution in the hyperfine field does not allow us to say that this component is 100% hematite. We cannot rule out the presence of maghemite and/or goethite in very small quantities. For the majority component (88%) described by a quadrupole splitting distribution, the values of the hyperfine parameters are very close to those of the non-magnetically ordered oxyhydroxide compounds at 293 K (FeOOH), if we exclude any phenomenon of superparamagnetism of fine grains [49]. The width of the quadrupole burst distribution is important and gives the signature of significant disorder around the studied iron probe. To best characterise this component, a low-speed study was carried out. With this velocity scale (Figure 9a), the contribution of the magnetically ordered component can be neglected (the most intense lines of the six-fold signal being located outside the analysis window). The experimental

spectrum then appears to consist of a single component represented by a distribution of quadrupole doublets (Dis.2). The refinement of the spectrum confirms the presence of a single site of trivalent, high-spin iron [50, 51]. These results confirm the results obtained at high speeds. The experimental spectrum consists of two components: a majority magnetically ordered component represented by a distribution of sextuplets (Dis.1) and a minor component represented by a quadrupole doublet (Site.2). The heat treatment significantly altered the distribution of iron in the laterite, compared to the previous spectrum. The refinement of the spectrum leads to isomeric displacement values that allow confirmation that the two components are related to trivalent, high spin iron. For the majority component (97%), the values of the hyperfine parameters ($\delta = 0.37$ mm/s, $\varepsilon = -0.11$ mm/s and $B_{hf}^{max} = 50$ T) are very similar to those of hematite. In this case, it would seem that only hematite is present in this heat-treated laterite. Concerning the minority component (3%), the values of the hyperfine parameters are very close to those determined during the study of the starting compound LAC (paramagnetic component Dis.2). Given its very low percentage, this could be an impurity of residual raw material.

When LAC600 was consolidated with alkaline solution, namely sample LACAS, the experimental spectrum consisted of two components: a majority magnetically ordered component represented by a distribution of sextuplets (Dis.1), and a minority component represented by a quadrupolar doublet (Site.2). The refinement of the spectrum leads to isomeric displacement values that allow us to refine that the two components are relative to high-spin, trivalent iron. For the majority component (Dis.1), the values of the hyperfine parameters ($\delta = 0.37$ mm/s, $\varepsilon = -0.11$ mm/s and $B_{hf}^{max} = 50$ T) (Table 4) are very similar to those of hematite. In this case, it would seem that only hematite is present in the alkali-activated laterite LACAS. For the minority component (Site.2), the values of the hyperfine parameters are very close to those determined during the study of the starting compound (LAC-Dis.2). Given its very low content, it can be considered as an impurity.

In a phosphoric acid medium, the experimental spectrum consists of three components: a majority magnetically ordered component represented by a distribution of sextuplets (Dis.1) and two more complex components represented by two distinct distributions of quadrupole doublets (Dis.2 and Dis.3). The refinement of the spectrum leads to isomeric displacement values that confirm that the three components are related to trivalent, high spin iron in 6-fold coordination [51]. The acid treatment of LAC600 drastically altered the spectrum, and therefore

has significantly altered the distribution of iron between the various contributions. For the Dis.1 component, as before, the values of the hyperfine parameters ($\delta = 0.36$ mm/s, $\varepsilon = -0.10$ mm/s and $B_{hf}^{max} = 50$ T) are very similar to those of hematite. However, the very large dispersion of the distribution in the hyperfine field does not confirm that this component is 100% hematite. The shape of the distribution around 50T could be a sign of the presence of another magnetically ordered component with a slightly weaker field (48-49 T), that could be due, for example, to maghemite in small quantities. For the Dis.2 component (13%), the hyperfine parameters are significantly different from those determined for the starting compound (LAC600-Dis.2); thus, the iron environment described by this component appears very different from that of the starting compound LAC600. The isomeric displacement value (0.43 mm/s) seems to indicate the presence of phosphate around iron. Further to this, the distribution of quadrupole splitting is very wide, which is the signature of a major disorder around the probed iron. Finally, the third and last component Dis.3 is very much in the minority (3%) and not magnetically ordered, and is quite similar to that determined for the compound before chemical treatment (LAC600-Dis.2).

3.2.4.2 Mössbauer spectra of LAI, LAI600, LAIAS and LAIPA samples

Table 5 presents the fitting results and Figure 9b displays the Mössbauer spectra of unheated iron-rich laterite (LAI), the corresponding calcined laterites (LAI600), and the resulting inorganic polymer binders, LAIAS and LAIPA. For the uncalcined iron-rich laterite (LAI), the experimental spectrum consists of two components: a highly distorted complex component (more or less magnetically ordered at room temperature), represented by a distribution of sextuplets (Dis.1), and a paramagnetic component represented by a distribution of quadrupolar doublets (Dis.2). The refinement of the spectrum leads to isomeric displacement values that allow confirmation that the two components are related to trivalent, high spin iron (Table 5). In this laterite (LAI), distinct from the LAC laterite, the percentage contributions of these two components are each close to 50%. For the Dis.1 component, as previously noted, the values of the hyperfine parameters ($\delta = 0.36$ mm/s, $\varepsilon = -0.10$ mm/s and $B_{hf}^{max} = 51$ T) are very similar to those of hematite. However, the very large dispersion of the distribution in hyperfine fields does not enable confirmation that this component is 100% hematite. The shape of the distribution of hyperfine fields, with values around 30 T, does not rule out the presence of goethite ($B_{hf} = 30$ T). For the second component Dis.2, the values of the hyperfine parameters are close to those determined during the study of the raw LAC, but also display characteristics (showing similar

δ and Δ values to those of α -FeOOH) of non-magnetically ordered oxyhydroxide compounds at 293 K (FeOOH), if any superparamagnetic phenomenon of fine grains is excluded.

After calcination at 600°C, the experimental spectrum consists of two components: a majority component (98%), magnetically ordered by a distribution of sextuplets (Dis.1), and a minority component (2%), represented by a quadrupolar doublet (Site.2). The heat treatment significantly altered the distribution of iron in the laterite (compared to the previous spectrum). The refinement of the spectrum leads to isomeric displacement values which confirm that the two components are related to trivalent, high spin iron. For the majority component (Dis.1), described by a sextuplet distribution, the values of the hyperfine parameters ($\delta = 0.37$ mm/s, $\epsilon = -0.11$ mm/s and $B_{hf}^{max} = 51$ T) are very similar to those of hematite. However, the difference spectrum (the difference between the experimental data and the calculated data) seems to indicate the presence of small quantities of another magnetically ordered compound (at room temperature), such as maghemite; the presence of this phase was also confirmed by XRD analysis above. The presence of (magnetically ordered) goethite cannot be identified, as in the case of the LAI starting compound leading to the transformation of goethite into hematite after calcination. Concerning the minority component (Site.2), the values of the hyperfine parameters are once more close to those determined for the raw material (LAI-Dis.2) as an impurity.

When LAI600 is consolidated with an alkaline solution (LAIAS), the experimental spectrum consists of two components: a magnetically ordered majority component described by a distribution of sextuplets (Dis.1) and a minority component represented by a distribution of quadrupolar doublets (Dis.2). The refinement of the spectrum leads to isomeric displacement values indicating that the two components are related to trivalent high spin iron. For the majority component (Dis.1), the values of the hyperfine parameters ($\delta = 0.37$ mm/s, $\epsilon = -0.10$ mm/s and $B_{hf}^{max} = 50$ T) are very similar to those of hematite. As with the LAI600 sample, the difference spectrum seems to indicate the presence in small quantities of another magnetically ordered compound (at room temperature), which cannot be goethite based on its hyperfine parameters, and is probably maghemite. For the minority component (Dis.2), the values of the hyperfine parameters are close to those determined during the initial study of the starting compound (LAI600 - Site.2) as an impurity. The reaction with the alkaline activator has not induced major changes in the coordination characteristics of the observable iron sites in LAIAS compared to LAI600.

When LAI600 is reacted in a phosphoric acid medium (LAIPA), the measured Mössbauer spectrum consists of three components: a majority component magnetically ordered by a distribution of sextuplets (Dis.1) and two very minor components represented by two distinct distributions of quadrupolar doublets (Dis.2 and Dis.3). The refinement of the spectrum leads to isomeric displacement values that again confirm that the two components are related to trivalent, high spin iron. The acidic treatment of LAI600 drastically altered the spectrum and therefore the distribution of iron environments. For the majority component (Dis.1), once again, the values of the hyperfine parameters ($\delta = 0.36$ mm/s, $\epsilon = -0.10$ mm/s and $B_{hf}^{max} = 50$ T) are very similar to those of hematite, but the very large dispersion of the distribution in hyperfine fields does not enable confirmation that this component is 100% hematite. The shape of the distribution around 50 T could be due to the presence of another magnetically ordered component in small quantities, such as maghemite, characterized by a weaker field (48-49 T). The second component (Dis.2) is very different from those observed for the LAI600 sample. It is characterized by a displacement of 0.47 mm/s, indicating the possible presence of phosphate around iron [52], and by a very wide quadrupolar splitting distribution (characteristic of significant disorder around the iron probe studied). This component could be provided by iron released through the partial dissolution of hematite, because the third component (Dis.3) has similar characteristics to that observed for the initial laterite (LAI - Dis.2).

3.2.5 X-band electron paramagnetic resonance spectra

The electron paramagnetic resonance (EPR) spectral fits for the X-band, performed on raw materials and those consolidated in an acidic or basic medium, are presented in Figure 10. The spectra of the raw LAC and LAI laterites display two signal and three signals, respectively, at weak magnetic fields (1000-200 mT). These are attributable to iron-rich mineral phases such as goethite, hematite, ilmenite and maghemite (also confirmed by XRD analysis above). After calcination (600°C), these signals give rise to a large intense peak, more so in the LAI600 sample compared to that of LAC600 at around 1500 mT ($g = 8.80$ and 4.28), which is the result of dehydroxylation of hydrated iron phases and kaolinite [53, 54]; the latter reflecting the substitution of Fe^{3+} ions in place of Al^{3+} ions in kaolinite. After reaction in an alkaline medium, the signal at higher magnetic field around 3500 mT ($g = 2.004$) becomes much more pronounced, related to the centered paramagnetic defect, which is not observed for products reacted in an acidic medium. Ultimately, this pronounced peak reflects the establishment of Fe-O-P bonding, indicating the formation of phosphate phases such as $FePO_4$, as also indicated by the ^{57}Fe

Mössbauer spectra and X-ray diffractograms of the consolidated inorganic polymer binders as discussed above. The formation of these iron-phosphate phases contributes to the densification of the binder structure, resulting in the higher compressive strength achieved by these specimens.

4. Conclusions

In this research phosphoric acid and alkaline solutions were used as activators for synthesis of laterite based inorganic polymers from two calcined natural materials: a lateritic clay and an iron-rich laterite. The microstructure, and thus also mechanical properties and thermal conductivity, of the consolidated products are influenced by the type of activator used. The resulting specimens obtained by alkali-activation of the iron-rich laterite using sodium silicate solution developed lower compressive strength, due to the formation of a less compact microstructure containing micro-cracks, compared to the corresponding alkali-activated lateritic clay samples, which were dense and exhibited the highest strength. An increase in curing temperature from 20 to 40 °C led to a decrease in mechanical properties, indicated by the appearance of fissures within the matrix, linked to evaporation of water at early age. Conversely, the high strength achieved by phosphoric acid-activated samples might be due to the compact or dense structure and the formation of a disordered iron phosphate phase, such as berlinite (FePO_4), as confirmed by ^{57}Fe Mössbauer and EPR analysis. The FTIR spectra of acid-activated samples indicate either the incorporation of PO_4^{3-} units or replacement of Al^{3+} by Fe^{3+} in the tetrahedral inorganic polymer 3D network.

The high values of thermal conductivity measured for samples fabricated using phosphoric acid ($\leq 0.9 \text{ W/m.K}^{-1}$) compared to those made with an alkaline solution ($\leq 0.6 \text{ W/m.K}^{-1}$), are likely correlated to the improved connectivity observed between different particles and the binder phase from SEM analysis. The idea of phosphoric acid activation is fundamentally derived from the feasibility of forming new phosphate-containing phases that would not be formed during alkali-activation. By adding phosphate, the combination of Al, Si, Fe and P resulted in chemical reactivity to allow promotion of new binder phases, capable of developing a compact and dense matrix with very low porosity, yielding the high strength. These newly formed phases seem to be enhanced with increased curing temperature (from 20 to 40 °C), contrary to the trend observed in alkaline activation. Overall, the processes of activation of iron-rich laterite and lateritic clay are very different in acidic and alkaline media, even if the products

of these reaction processes are superficially similar in microstructure and in their crystallographically disordered nature.

5. Acknowledgements

RCK grateful acknowledges the financial support of AVRUL (Agence pour la Valorisation de la Recherche Universitaire du Limousin) for his stay in IRCER, UMRCNRS 7315, Limoges, France under 2018 AVRUL postgraduate internship. The authors also like to express gratitude to the Director of IRCER for having made accessible all accommodations for carrying out this work in the laboratory. This project also received the contribution of the FLAIR fellowship African Academic of Science and the Royal Society through the funding N° FLR/R1/201402. The participation of ASY and JLP has been supported by EPSRC through grant EP/T013524/1.

6. References

1. Kamseu, E., A. Nzeukou, P. Lemougna, N. Billong, U. Melo, and C. Leonelli, *Induration of Laterites in tropical areas: Assessment for potential structural applications*. InterCeram: International Ceramic Review, 2013. 62(6):430-437.
2. Lecomte-Nana, G., H. Goure-Doubi, A. Smith, A. Wattiaux, and G. Lecomte, *Effect of iron phase on the strengthening of lateritic-based "geomimetic" materials*. Applied Clay Science, 2012. 70: p. 14-21.
3. Sherman, G.D., *Factors influencing the development of lateritic and laterite soils in the Hawaiian Islands*. University of Hawaii Press, Pacific Science Volume 3, Number 4, 1949.
4. Goure-Doubi, H., G. Lecomte-Nana, F. Nait-Abbou, B. Nait-Ali, A. Smith, V. Coudert, and L. Konan, *Understanding the strengthening of a lateritic "geomimetic" material*. Construction and Building Materials, 2014. 55: p. 333-340.
5. Kasthurba, A.K., M. Santhanam, and M.S. Mathews, *Investigation of laterite stones for building purpose from Malabar region, Kerala state, SW India – Part 1: Field studies and profile characterisation*. Construction and Building Materials, 2007. 21(1): p. 73-82.
6. Kaze, R.C., L.M. Beleuk à Mougam, M.L. Fonkwe Djouka, A. Nana, E. Kamseu, U.F. Chinje Melo, and C. Leonelli, *The corrosion of kaolinite by iron minerals and the effects on geopolymerization*. Applied Clay Science, 2017. 138: p. 48-62.
7. Lemougna, P.N., A.B. Madi, E. Kamseu, U.C. Melo, M.-P. Delplancke, and H. Rahier, *Influence of the processing temperature on the compressive strength of Na activated lateritic soil for building applications*. Construction and Building Materials, 2014. 65: p. 60-66.
8. Davidovits, J. *Geopolymer Chemistry and Applications. 4-th edition*. Saint-Quentin, France. 2nd Nov 2015.
9. Wang, Y.-S., Y. Alrefaei, and J.-G. Dai, *Silico-Aluminophosphate and Alkali-Aluminosilicate Geopolymers: A Comparative Review*. Frontiers in Materials. 2019. 6(106):p 1-17.
10. Hounsi, A.D., G.L. Lecomte-Nana, G. Djétéli, and P. Blanchart, *Kaolin-based geopolymers: Effect of mechanical activation and curing process*. Construction and Building Materials, 2013. 42: p. 105-113.
11. Kaze, C.R., T. Alomayri, A. Hasan, S. Tome, G.L. Lecomte-Nana, J.G.D. Nemaleu, H.K. Tchakoute, E. Kamseu, U.C. Melo, and H. Rahier, *Reaction kinetics and rheological behaviour of meta-halloysite based geopolymer cured at room temperature: Effect of thermal activation*

- on physicochemical and microstructural properties*. Applied Clay Science, 2020. **196**: p. 105773.
12. Kaze, C.R., H.K. Tchakoute, T.T. Mbakop, J.R. Mache, E. Kamseu, U.C. Melo, C. Leonelli, and H. Rahier, *Synthesis and properties of inorganic polymers (geopolymers) derived from Cameroon-meta-halloysite*. Ceramics International, 2018. **44**(15): p. 18499-18508.
 13. Nana, A., J. Ngouné, R.C. Kaze, L. Boubakar, S.K. Tchounang, H.K. Tchakouté, E. Kamseu, and C. Leonelli, *Room-temperature alkaline activation of feldspathic solid solutions: Development of high strength geopolymers*. Construction and Building Materials, 2019. **195**: p. 258-268.
 14. Youmoue, M., R.T. Tene Fongang, A. Gharzouni, R.C. Kaze, E. Kamseu, V.M. Sglavo, I. Tonle Kenfack, B. Nait-Ali, and S. Rossignol, *Effect of silica and lignocellulosic additives on the formation and the distribution of meso and macropores in foam metakaolin-based geopolymer filters for dyes and wastewater filtration*. SN Applied Sciences, 2020. **2**(4): p. 642.
 15. Assaedi, H., T. Alomayri, C.R. Kaze, B.B. Jindal, S. Subaer, F. Shaikh, and S. Alraddadi, *Characterization and properties of geopolymer nanocomposites with different contents of nano-CaCO₃*. Construction and Building Materials, 2020. **252**: p. 119137.
 16. Mustakim, S.M., S.K. Das, J. Mishra, A. Aftab, T.S. Alomayri, H.S. Assaedi, and C.R. Kaze, *Improvement in Fresh, Mechanical and Microstructural Properties of Fly Ash- Blast Furnace Slag Based Geopolymer Concrete By Addition of Nano and Micro Silica*. Silicon, 2020.
 17. Bernal, S.A., J.L. Provis, B. Walkley, R. San Nicolas, J.D. Gehman, D.G. Brice, A.R. Kilcullen, P. Duxson, and J.S.J. van Deventer, *Gel nanostructure in alkali-activated binders based on slag and fly ash, and effects of accelerated carbonation*. Cement and Concrete Research, 2013. **53**: p. 127-144.
 18. Lemougna, P.N., U.F. Chinje Melo, M.-P. Delplancke, and H. Rahier, *Influence of the chemical and mineralogical composition on the reactivity of volcanic ashes during alkali activation*. Ceramics International, 2014. **40**(1, Part A): p. 811-820.
 19. Lemougna, P.N., K.J.D. MacKenzie, and U.F.C. Melo, *Synthesis and thermal properties of inorganic polymers (geopolymers) for structural and refractory applications from volcanic ash*. Ceramics International, 2011. **37**(8): p. 3011-3018.
 20. Boum, R.B.E., C.R. Kaze, J.G.D. Nemaleu, V.B. Djaoyang, N.Y. Rachel, P.L. Ninla, F.M. Owono, and E. Kamseu, *Thermal behaviour of metakaolin–bauxite blends geopolymer: microstructure and mechanical properties*. SN Applied Sciences, 2020. **2**(8): p. 1358.
 21. Peys, A., L. Arnout, B. Blanpain, H. Rahier, K. Van Acker, and Y. Pontikes, *Mix-design Parameters and Real-life Considerations in the Pursuit of Lower Environmental Impact Inorganic Polymers*. Waste and Biomass Valorization, 2018. **9**(6): p. 879-889.
 22. Hanjitsuwan, S., T. Phoo-ngernkham, L.-y. Li, N. Damrongwiriyanupap, and P. Chindapasirt, *Strength development and durability of alkali-activated fly ash mortar with calcium carbide residue as additive*. Construction and Building Materials, 2018. **162**: p. 714-723.
 23. Yankwa Djobo, J.N., A. Elimbi, H. Kouamo Tchakouté, and S. Kumar, *Mechanical properties and durability of volcanic ash based geopolymer mortars*. Construction and Building Materials, 2016. **124**: p. 606-614.
 24. Bewa, C.N., H.K. Tchakouté, C.H. Rüscher, E. Kamseu, and C. Leonelli, *Influence of the curing temperature on the properties of poly(phospho-ferro-siloxo) networks from laterite*. SN Applied Sciences, 2019. **1**(8): p. 916.
 25. Kamseu, E., C.R. Kaze, J.N.N. Fekoua, U.C. Melo, S. Rossignol, and C. Leonelli, *Ferrisilicates formation during the geopolymerization of natural Fe-rich aluminosilicate precursors*. Materials Chemistry and Physics, 2020. **240**: p. 122062.
 26. Kaze, C.R., J.N.Y. Djobo, A. Nana, H.K. Tchakoute, E. Kamseu, U.C. Melo, C. Leonelli, and H. Rahier, *Effect of silicate modulus on the setting, mechanical strength and microstructure of iron-rich aluminosilicate (laterite) based-geopolymer cured at room temperature*. Ceramics International, 2018. **44**(17): p. 21442-21450.

27. Kaze, C.R., P. Venyite, A. Nana, D.N. Juvenal, H.K. Tchakoute, H. Rahier, E. Kamseu, U.C. Melo, and C. Leonelli, *Meta-halloysite to improve compactness in iron-rich laterite-based alkali activated materials*. *Materials Chemistry and Physics*, 2020. **239**: p. 122268.
28. Kaze, R.C., L.M. Beleuk à Mougam, M. Cannio, R. Rosa, E. Kamseu, U.C. Melo, and C. Leonelli, *Microstructure and engineering properties of Fe₂O₃(FeO)-Al₂O₃-SiO₂ based geopolymer composites*. *Journal of Cleaner Production*, 2018. **199**: p. 849-859.
29. Lassinantti Gualtieri, M., M. Romagnoli, S. Pollastri, and A.F. Gualtieri, *Inorganic polymers from laterite using activation with phosphoric acid and alkaline sodium silicate solution: Mechanical and microstructural properties*. *Cement and Concrete Research*, 2015. **67**: p. 259-270.
30. Lecomte-nana, G.L., E. Lesueur, J.P. Bonnet, and G. Lecomte, *Characterization of a lateritic geomaterial and its elaboration through a chemical route*. *Construction and Building Materials*, 2009. **23**(2): p. 1126-1132.
31. Nkwaju, R.Y., J.N.Y. Djobo, J.N.F. Nouping, P.W.M. Huisken, J.G.N. Deutou, and L. Courard, *Iron-rich laterite-bagasse fibers based geopolymer composite: Mechanical, durability and insulating properties*. *Applied Clay Science*, 2019. **183**: p. 105333.
32. Gomes, K.C., G.S.T. Lima, S.M. Torres, S.R. de Barros, I.F. Vasconcelos, and N.P. Barbosa, *Iron Distribution in Geopolymer with Ferromagnetic Rich Precursor*. *Materials Science Forum*, 2010. **643**: p. 131-138.
33. Lawther, S., J. McIntosh, S. Nanukuttan, J. Provis, M. Soutsos, and D. Jose. *Understanding the microstructure of alternative binder systems—banahCEM, a metakaolin based geopolymer*. *Civil Engineering Research in Ireland*. 2016.
34. Hu, Y., S. Liang, J. Yang, Y. Chen, N. Ye, Y. Ke, S. Tao, K. Xiao, J. Hu, H. Hou, W. Fan, S. Zhu, Y. Zhang, and B. Xiao, *Role of Fe species in geopolymer synthesized from alkali-thermal pretreated Fe-rich Bayer red mud*. *Construction and Building Materials*, 2019. **200**: p. 398-407.
35. Bourret, J., N. Tessier-Doyen, B. Naït-Ali, F. Pennec, A. Alzina, C.S. Peyratout, and D.S. Smith, *Effect of the pore volume fraction on the thermal conductivity and mechanical properties of kaolin-based foams*. *Journal of the European Ceramic Society*, 2013. **33**(9): p. 1487-1495.
36. Hesse, J. and A. Rubartsch, *Model independent evaluation of overlapped Mossbauer spectra*. *Journal of Physics E: Scientific Instruments*, 1974. **7**(7): p. 526-532.
37. Mestdagh, M.M., L. Vielvoye, and A.J. Herbillon, *Iron in kaolinite: II. The relationship between kaolinite crystallinity and iron content*. *Clay Minerals*, 1980. **15**(1): p. 1-13.
38. Mendelovici, E., R. Villalba, and S. Yariv, *Iron-Bearing Kaolinite in Venezuelan Laterites. II. DTA and Thermal Weight Losses of KCl and CsCl Mixtures of Laterites*. *Israel Journal of Chemistry*, 1982. **22**(3): p. 247-252.
39. White, C.E., J.L. Provis, T. Proffen, D.P. Riley, and J.S.J. van Deventer, *Density Functional Modeling of the Local Structure of Kaolinite Subjected to Thermal Dehydroxylation*. *The Journal of Physical Chemistry A*, 2010. **114**(14): p. 4988-4996.
40. Lecomte-Nana, G., J.-P. Bonnet, and N. Soro, *Influence of iron onto the structural reorganization process during the sintering of kaolins*. *Journal of the European Ceramic Society*, 2013. **33**(4): p. 661-668.
41. Bayiha, B.N., N. Billong, E. Yamb, R.C. Kaze, and R. Nzengwa, *Effect of limestone dosages on some properties of geopolymer from thermally activated halloysite*. *Construction and Building Materials*, 2019. **217**: p. 28-35.
42. Chavda, M.A., S.A. Bernal, D.C. Apperley, H. Kinoshita, and J.L. Provis, *Identification of the hydrate gel phases present in phosphate-modified calcium aluminate binders*. *Cement and Concrete Research*, 2015. **70**: p. 21-28.
43. Djobo, J.N.Y., D. Stephan, and A. Elimbi, *Setting and hardening behavior of volcanic ash phosphate cement*. *Journal of Building Engineering*, 2020. **31**: p. 101427.

44. Mimboe, A.G., M.T. Abo, J.N.Y. Djobo, S. Tome, R.C. Kaze, and J.G.N. Deutou, *Lateritic soil based-compressed earth bricks stabilized with phosphate binder*. Journal of Building Engineering, 2020. **31**: p. 101465.
45. Wang, Y.-S., J.L. Provis, and J.-G. Dai, *Role of soluble aluminum species in the activating solution for synthesis of silico-aluminophosphate geopolymers*. Cement and Concrete Composites, 2018. **93**: p. 186-195.
46. Wang, Y.-S., J.-G. Dai, Z. Ding, and W.-T. Xu, *Phosphate-based geopolymer: Formation mechanism and thermal stability*. Materials Letters, 2017. **190**: p. 209-212.
47. Han, Y., X. Cui, X. Lv, and K. Wang, *Preparation and characterization of geopolymers based on a phosphoric-acid-activated electrolytic manganese dioxide residue*. Journal of Cleaner Production, 2018. **205**: p. 488-498.
48. Lewandowska, J., M. Staszewska, M. Kepczynski, M. Szuwarzyński, A. Łatkiewicz, Z. Olejniczak, and M. Nowakowska, *Sol-gel synthesis of iron oxide-silica composite microstructures*. Journal of Sol-Gel Science and Technology, 2012. **64**(1): p. 67-77.
49. Goure Doubi, B.I.H., *Etude de la consolidation des matériaux "géomimétiques" à base d'argile latéritique : effet des acides et des phases ferriques*. 2013. p. 1 vol. (185 p.).
50. Peys, A., A.P. Douvalis, V. Hallet, H. Rahier, B. Blanpain, and Y. Pontikes, *Inorganic Polymers From CaO-FeOx-SiO2 Slag: The Start of Oxidation of Fe and the Formation of a Mixed Valence Binder*. 2019. **6**(212).
51. Battle, P.D., T.C. Gibb, G. Hu, D.C. Munro, and J.P. Atfield, *The magnetic properties of the high pressure phase of ferric phosphate, FePO₄-II*. Journal of Solid State Chemistry, 1986. **65**(3): p. 343-350.
52. Lin, R., A.P. Amrute, F. Krumeich, K. Lázár, R. Hauert, M. Yulikov, and J. Pérez-Ramírez, *Phase-controlled synthesis of iron phosphates via phosphorylation of β-FeOOH nanorods*. CrystEngComm, 2016. **18**(18): p. 3174-3185.
53. Muller, J.-P. and G.J.E.G. Calas, *Tracing kaolinites through their defect centers; kaolinite paragenesis in a laterite (Cameroon)*. Economic Geology. 1989. **84**(3): p. 694-707.
54. Vassilikou-Dova, A.B.J.A.M., *EPR-determined site distributions of low concentrations of transition-metal ions in minerals: Review and predictions*. American Mineralogist (1993) **78** (1-2): 49-55.

Figure captions

Figure 1. Synthesis protocol of consolidated activated laterites based geomaterials.

Figure 2a. Diffractograms of uncalcined (LAI) and calcined (LAI600) iron-rich laterites.

Figure 2b. Diffractograms of uncalcined (LAC) and calcined (LAC600) lateritic clays.

Figure 3a. TG and DTA curves of raw lateritic clay (LAC).

Figure 3b. TG and DTA curves of raw iron-rich laterite (LAI)

Figure 4a. Infrared spectra of uncalcined (LAC) and calcined (LAC600) lateritic clays.

Figure 4b. Infrared spectra of uncalcined (LAI) and calcined (LAI600) iron-rich laterites.

Figure 5a. X-ray patterns of calcined lateritic clay (LAC600) and laterite based inorganic polymer binders LACAS and LACPA. Key: quartz (SiO₂, (Q) PDF# 00-046-1045); hematite (α-Fe₂O₃, (He) PDF # 04-003-2900); berlinite (FePO₄ (B) PDF# 00-010-0423).

Figure 5b. X-ray patterns of calcined lateritic clay (LAI600) and laterite based inorganic polymer binders LAIAS and LAIPA. Key: Q (quartz SiO₂, PDF# 00-046-1045); H (hematite,

α -Fe₂O₃, PDF # 04-003-2900), maghemite (γ -Fe₂O₃, PDF# 01-084-1595), iron hydrogen phosphate hydrate (Fe₃H₁₅(PO₄)₈·4H₂O (Np), PDF# 00-045-0502), berlinite (FePO₄ (B), PDF# 00-010-0423), ferrowyllieite (AlFe₂Na₂(PO₄)₃ (Fi), PDF# 00-051-0508), sodium iron phosphate (Na₃Fe₂(PO₄)₃ (Sp), PDF# 00-045-0319) and iron phosphate hydroxide (Fe₄(PO₄)₃(OH)₃, PDF# 00-047-0413).

Figure 6a. Infrared spectra of calcined iron-rich laterite (LAI600) and laterite based inorganic polymers LAIAS and LAIPA.

Figure 6b. Infrared spectra of calcined lateritic clay (LAC600) and laterite based inorganic polymers LACAS and LACPA.

Figure 7a. TGA curves of consolidated laterite based inorganic polymers using alkaline and acid solutions.

Figure 7b. DTA curves of consolidated laterite based inorganic polymers using alkaline and acid solutions.

Figure 8a. SEM images of LACPA and LACAS samples cured at 20 °C.

Figure 8b. SEM images of LAIAS and LAIPA samples cured at 20 °C.

Figure 8c. SEM images of LACAS and LAIAS samples cured at 40 °C.

Figure 8d. Micrographs and EDS spectra of laterite based inorganic polymer LAIPA cured at 40 °C.

Figure 9a. Mössbauer spectra of LAC, LAC600, LACAS and LACPA samples.

Figure 9b. Mössbauer spectra of LAI, LAI600, LAIAS and LAIPA samples.

Figure 10. X-band electron paramagnetic resonance (EPR) spectra of raw and geomaterial samples.

Tables caption

Table 1. Chemical composition of raw and calcined laterites.

Table 2. Compressive strength of laterite-based inorganic polymer cured at 20 and 40 °C using alkaline solution (AS) and phosphoric acid (PA).

Table 3. Thermal conductivity, open porosity and water absorption values.

Table 4. Hyperfine parameters obtained from fitting of Mössbauer spectra of LAC, LAC600, LACAS and LACPA samples.

Table 5. Hyperfine parameters obtained from fitting of Mössbauer spectra of LAI, LAI600, LAIAS and LAIPA samples.

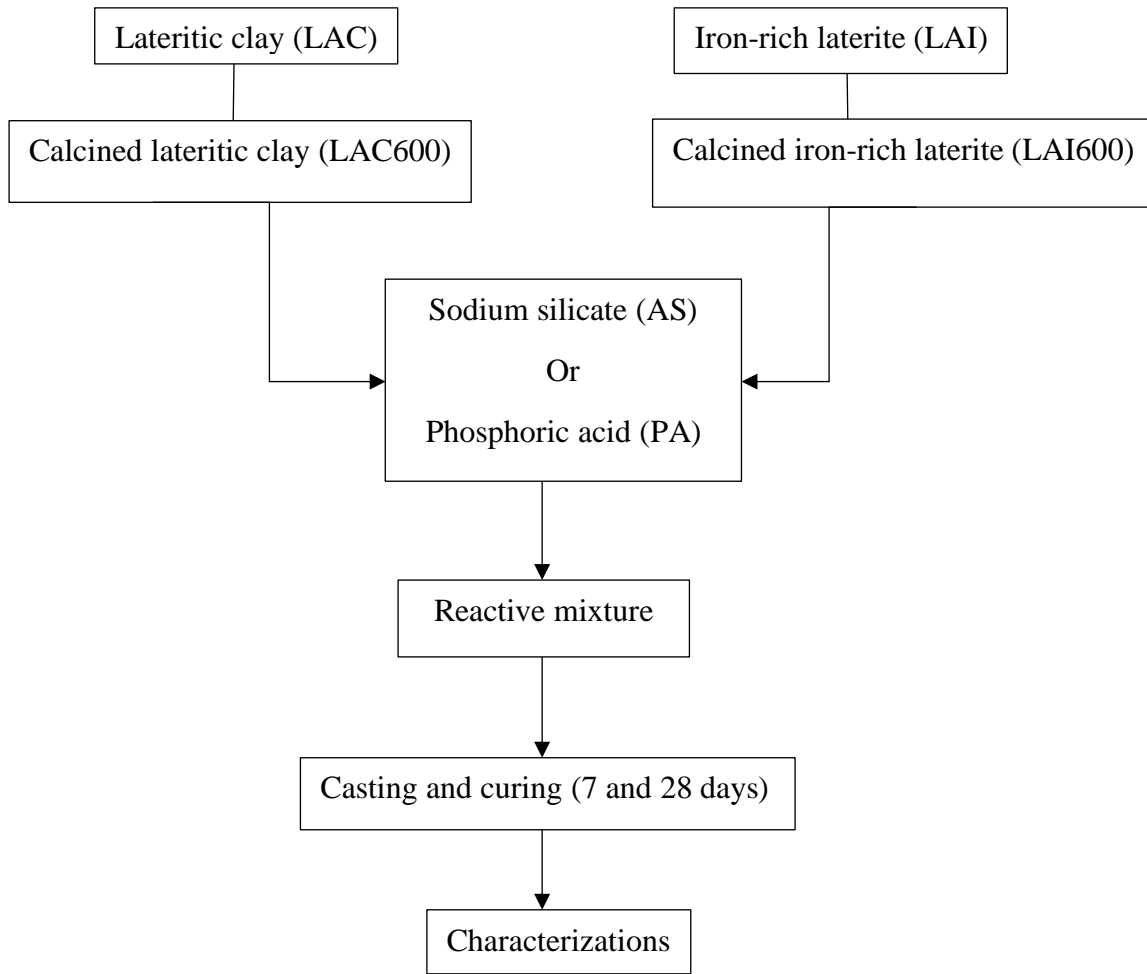
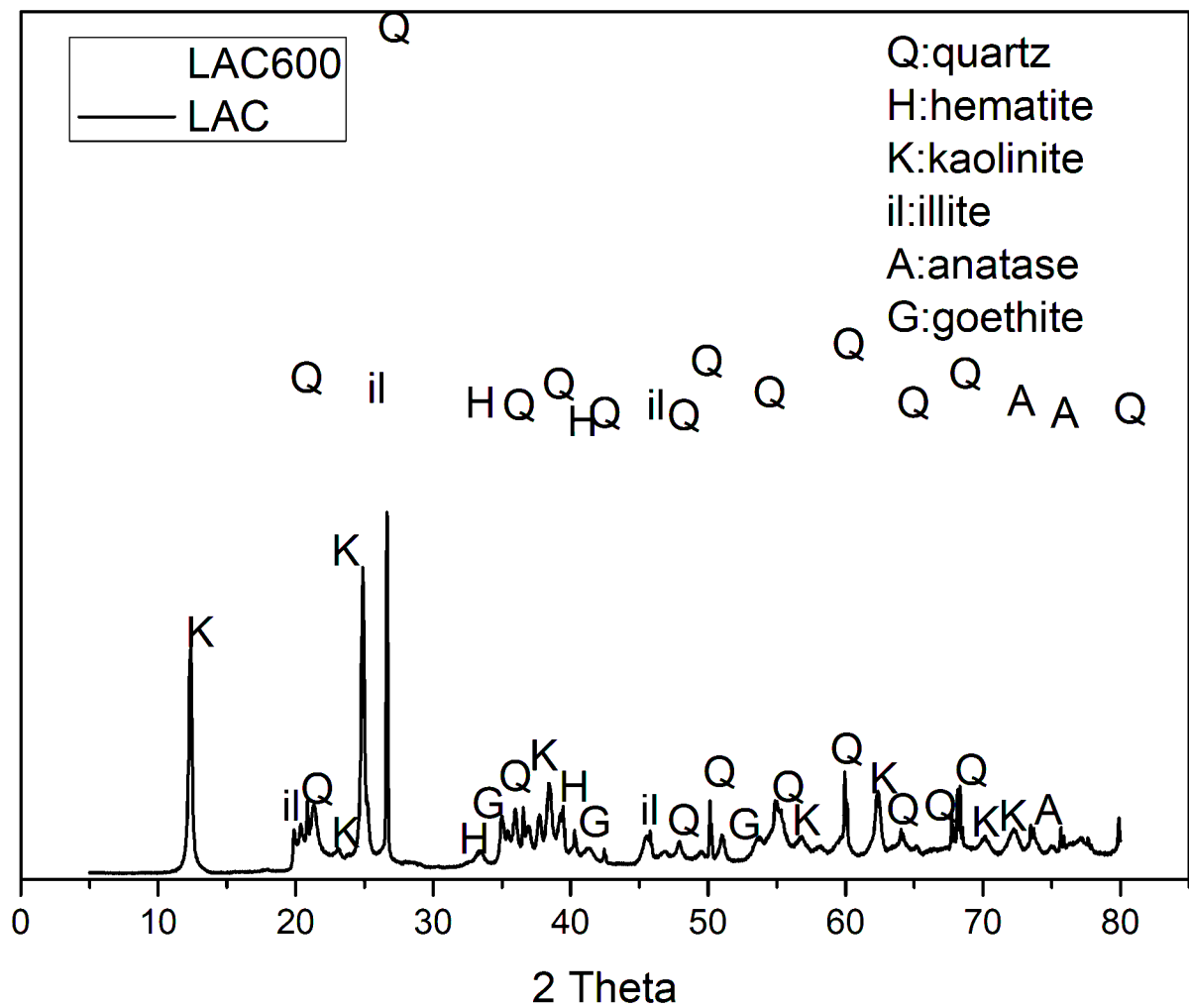
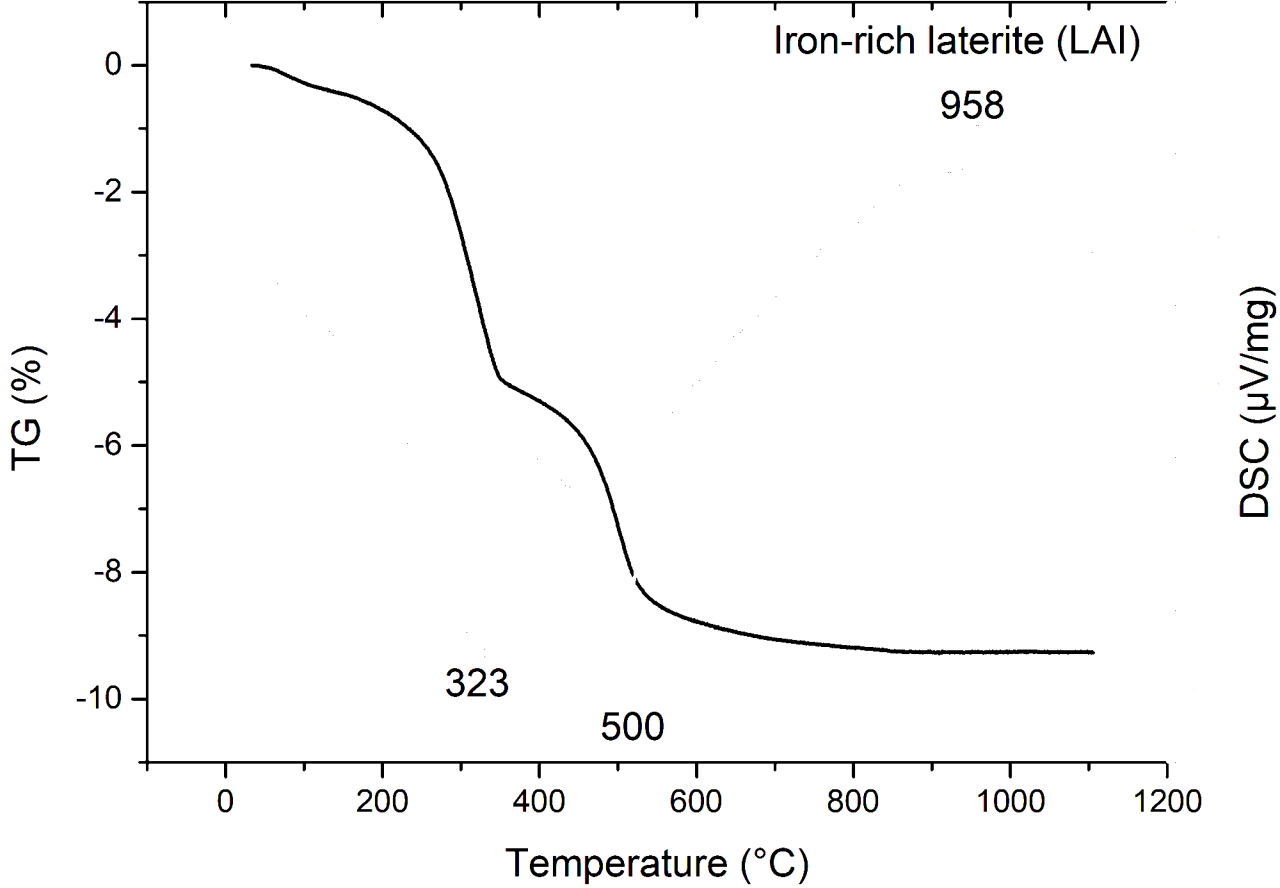
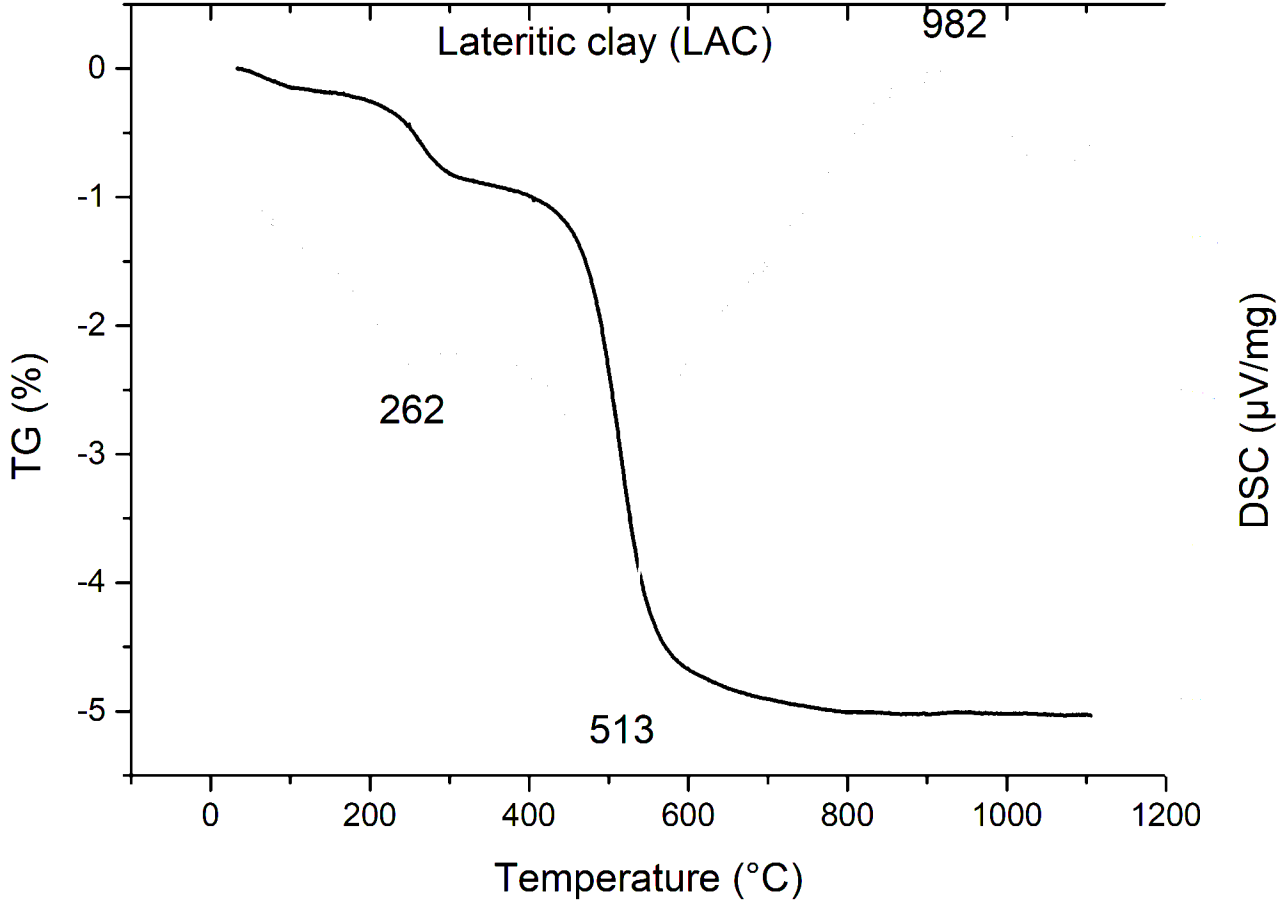


Figure 1.

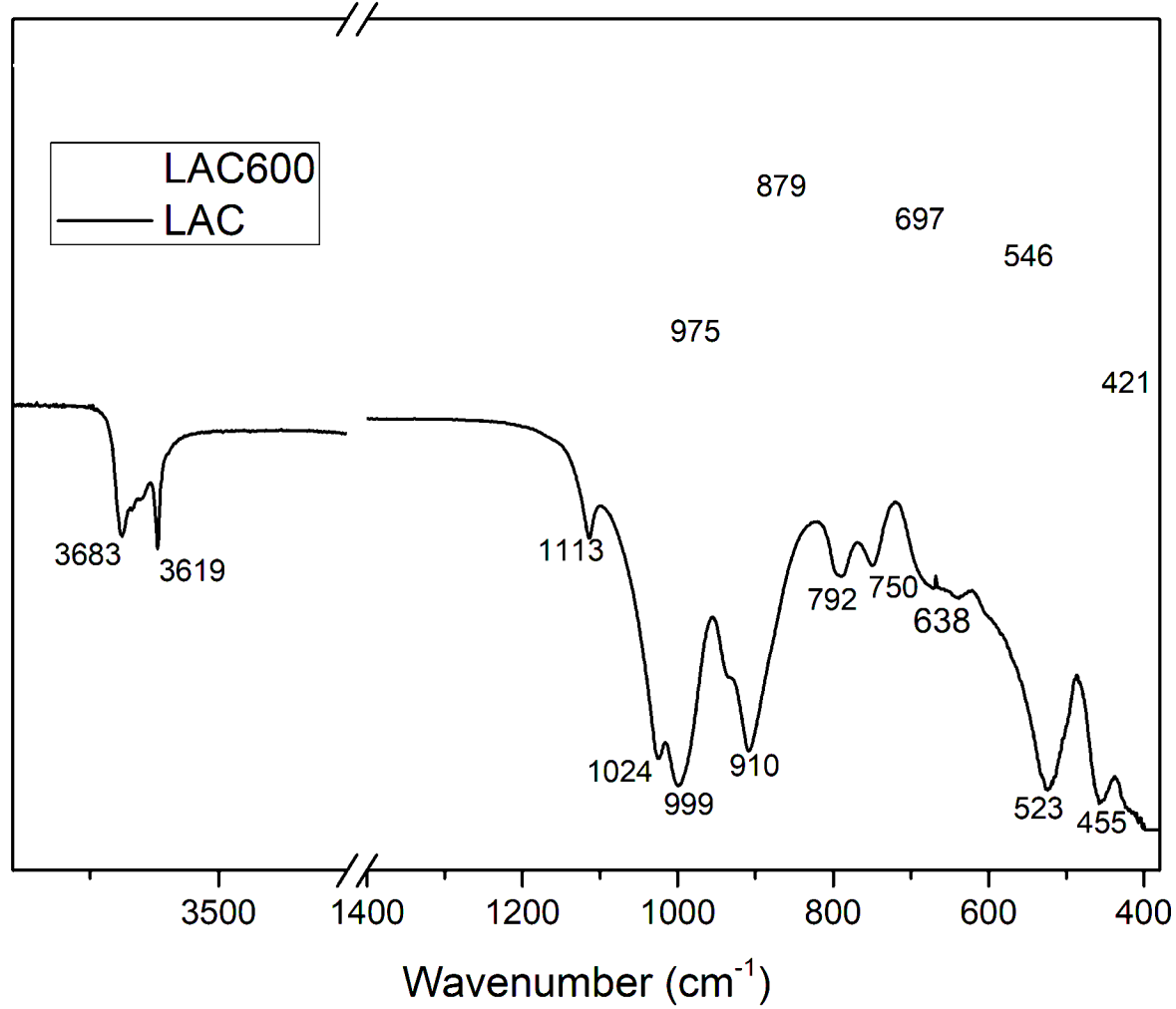
Relative intensity (a.u)



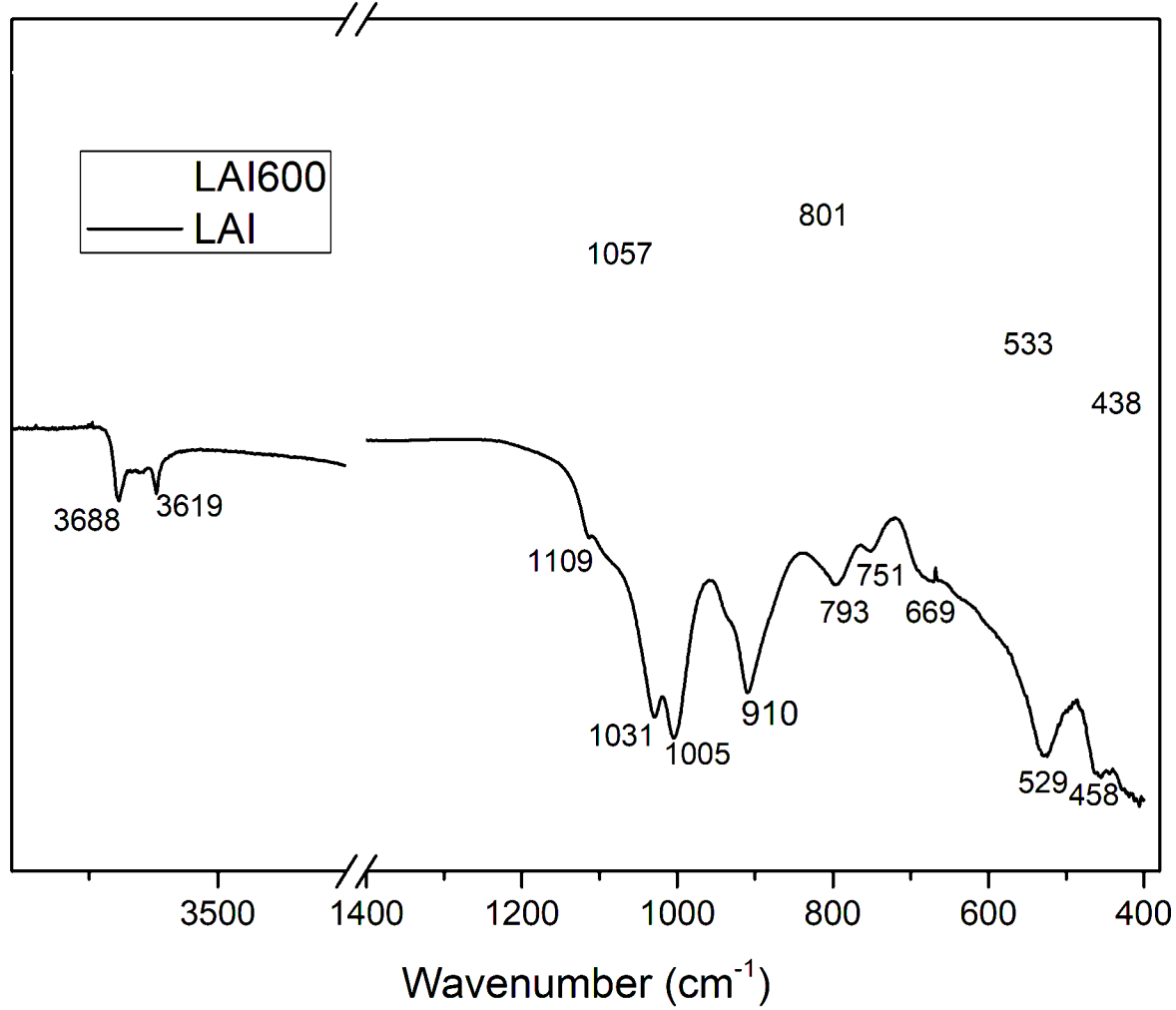


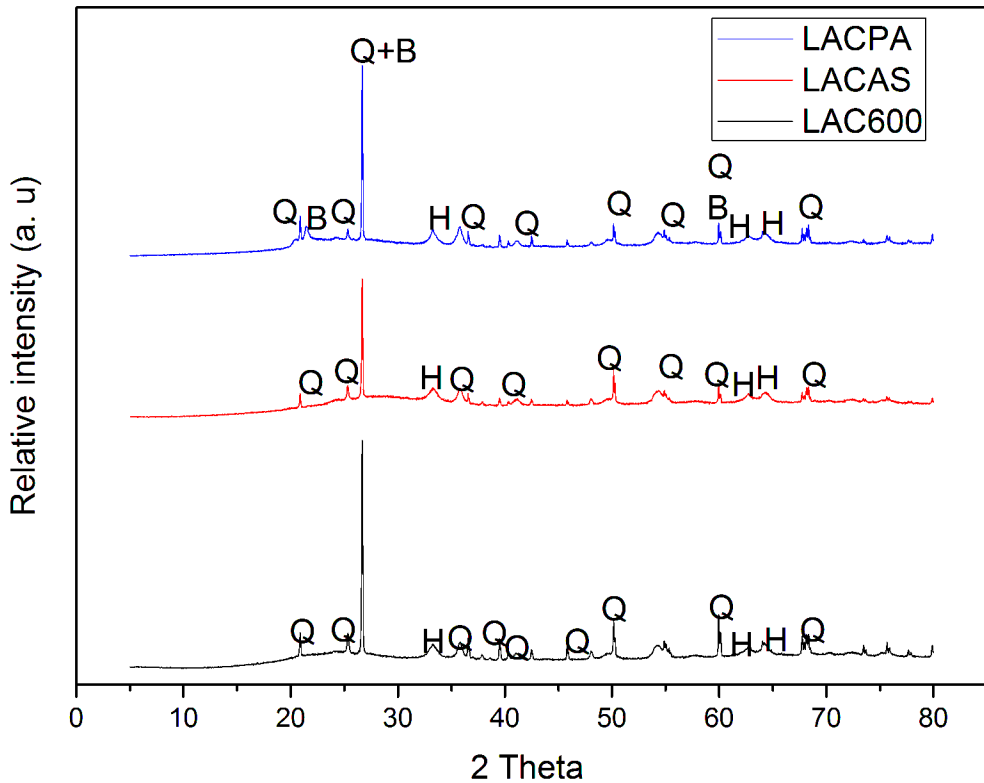


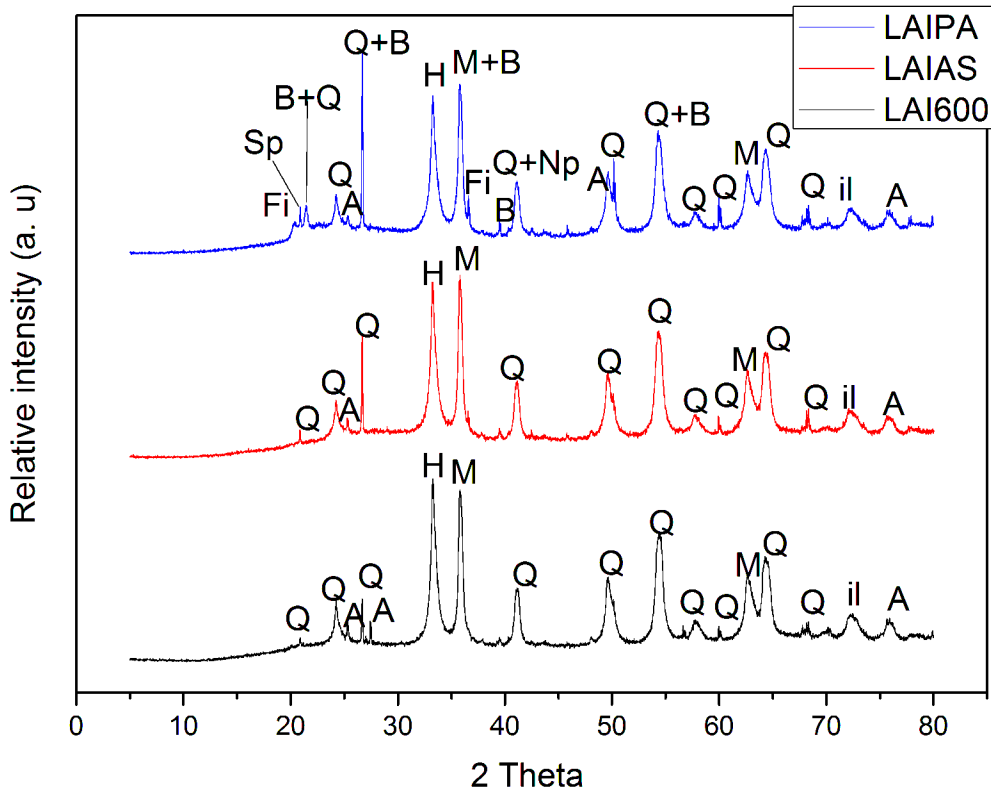
Transmittance (arb. units)

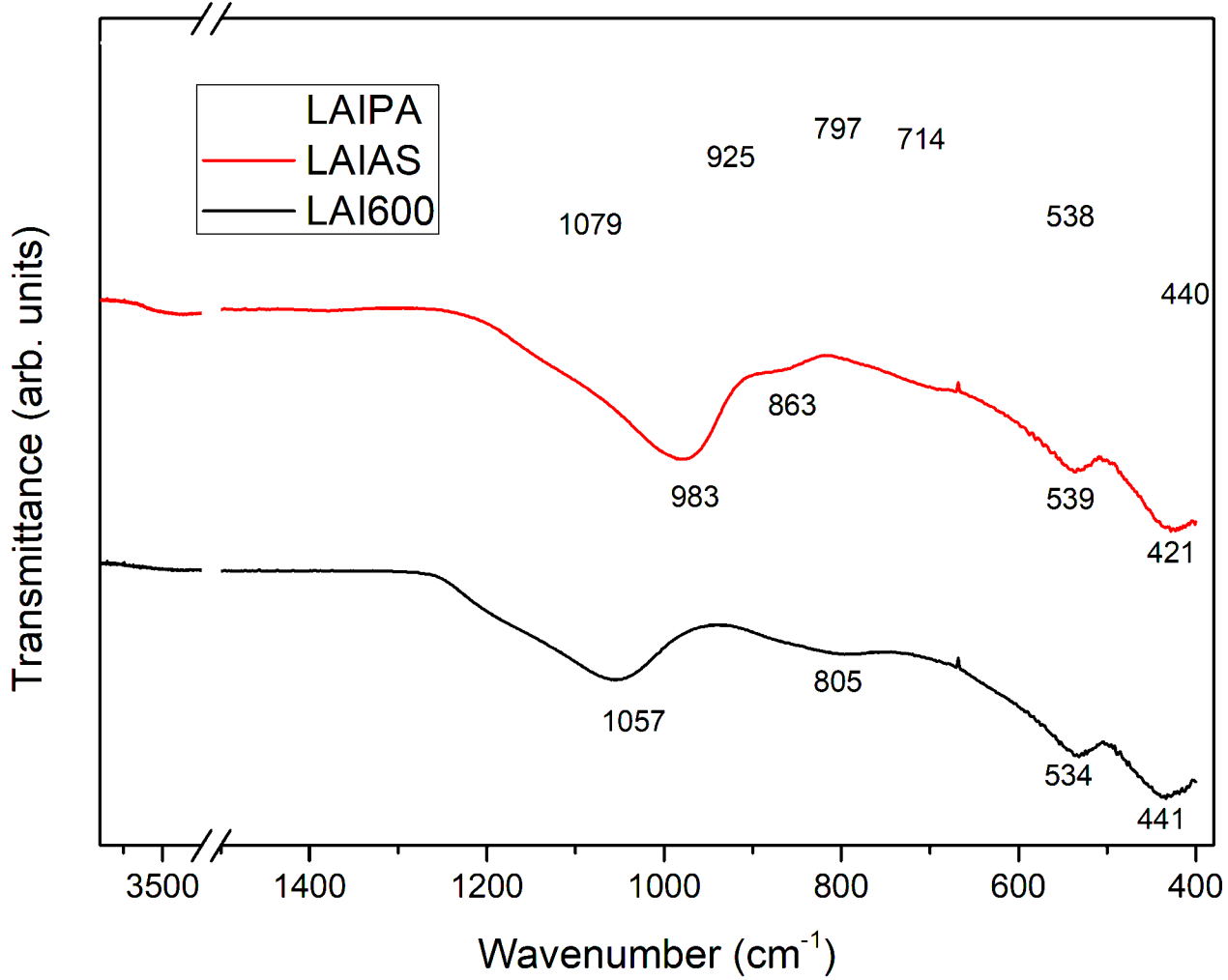


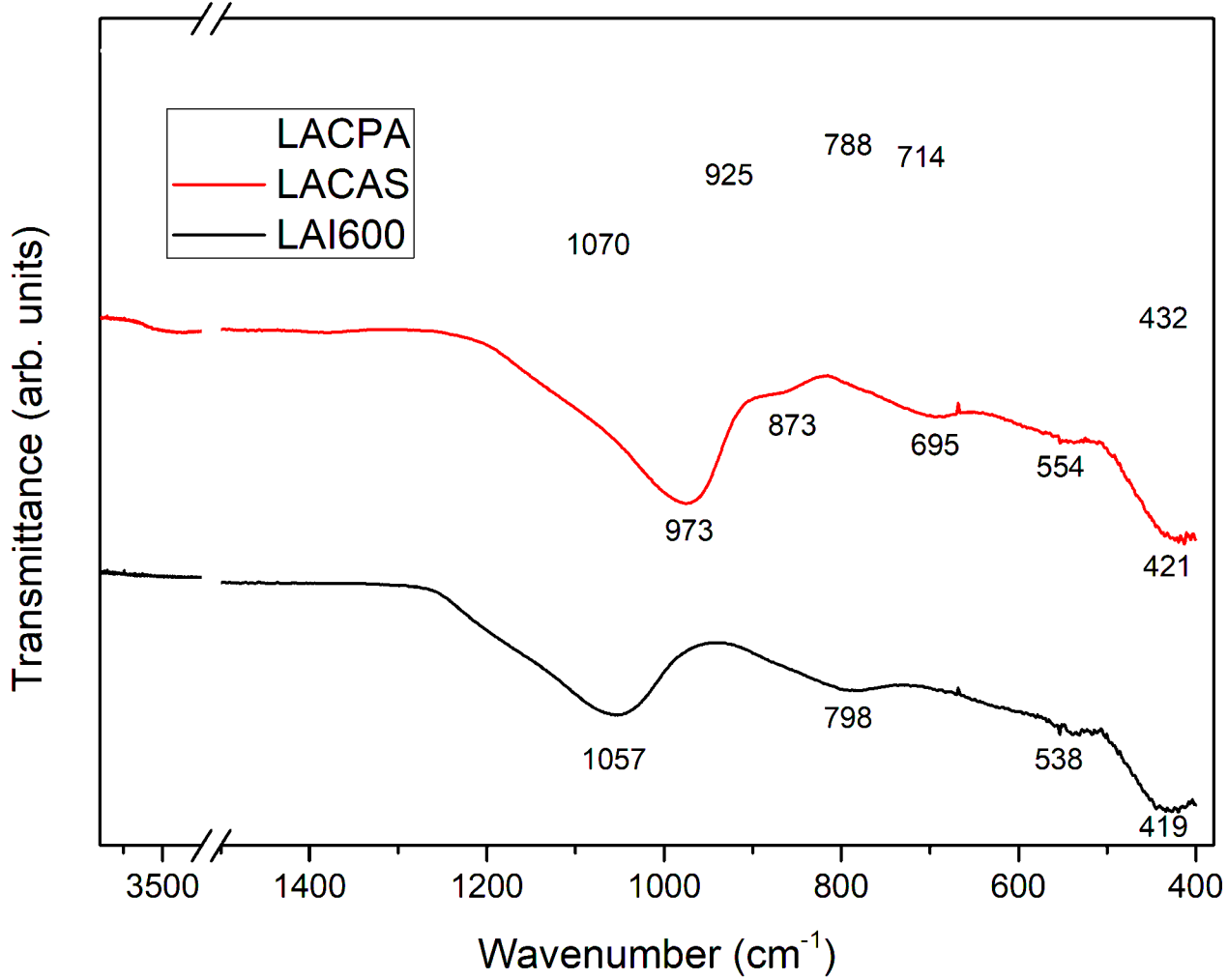
Transmittance (arb. units)

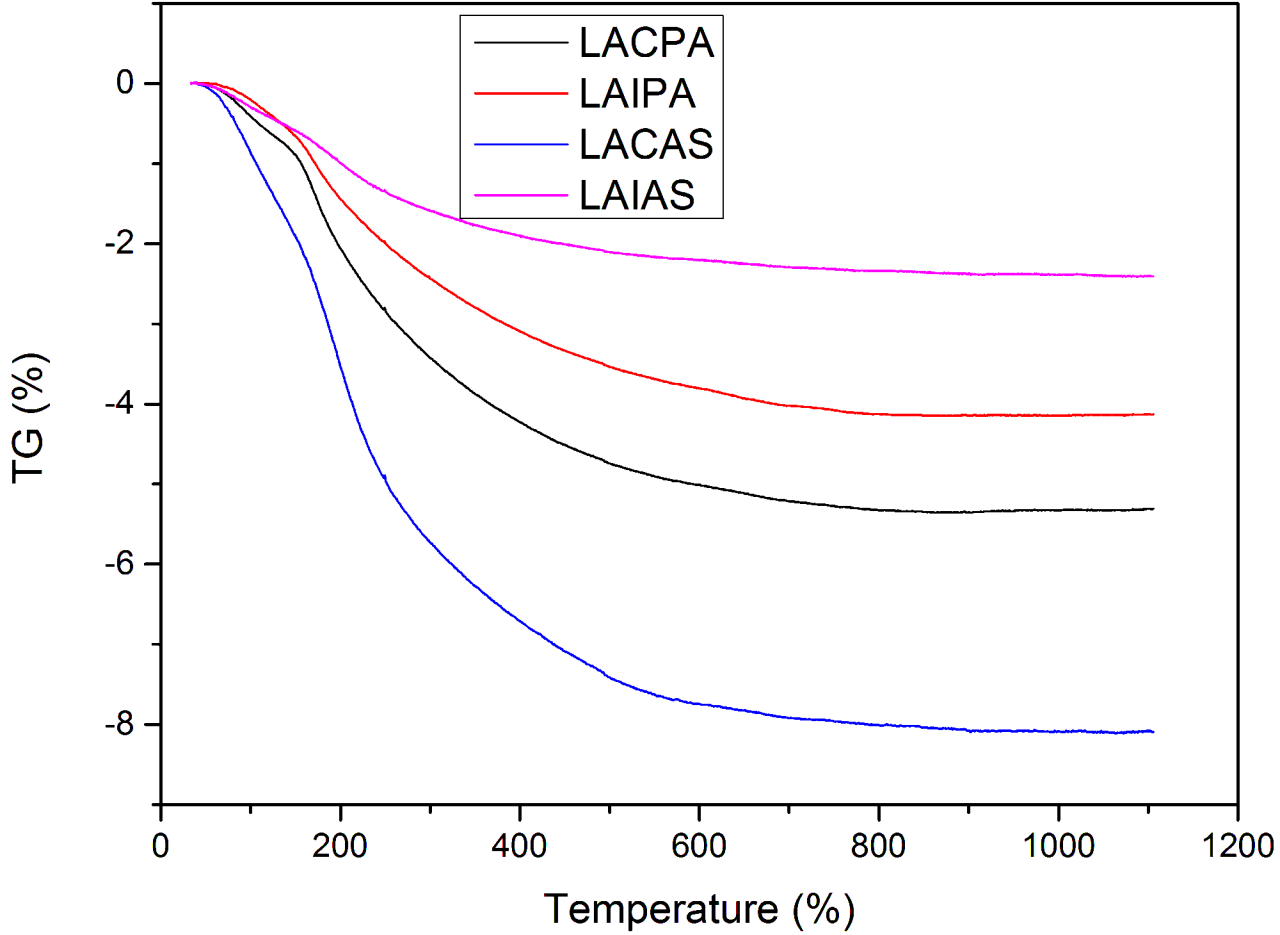


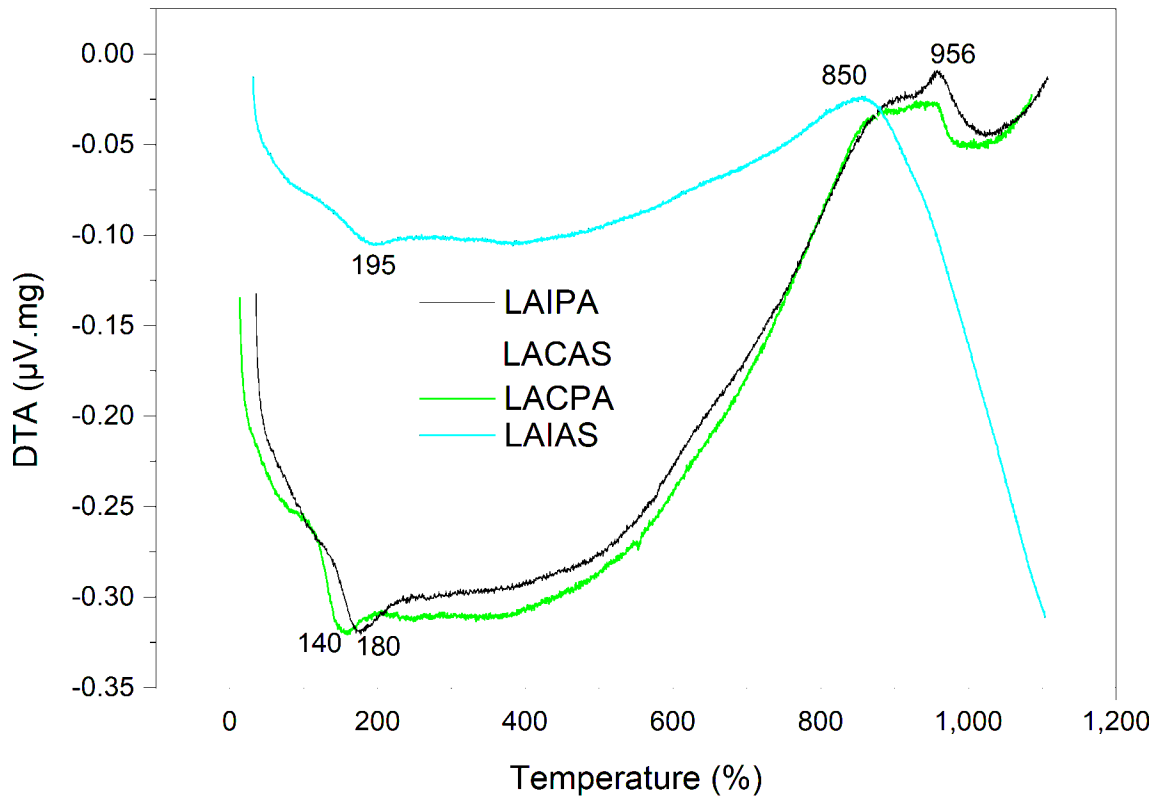


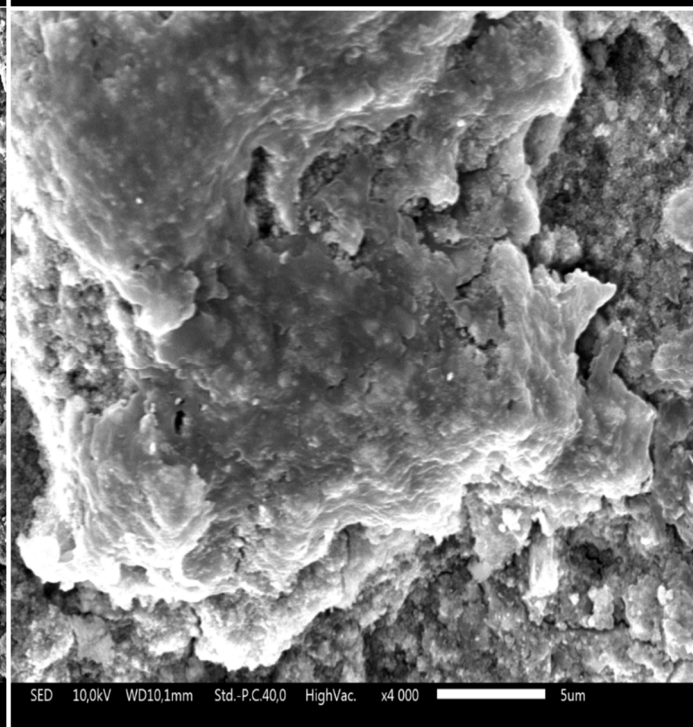
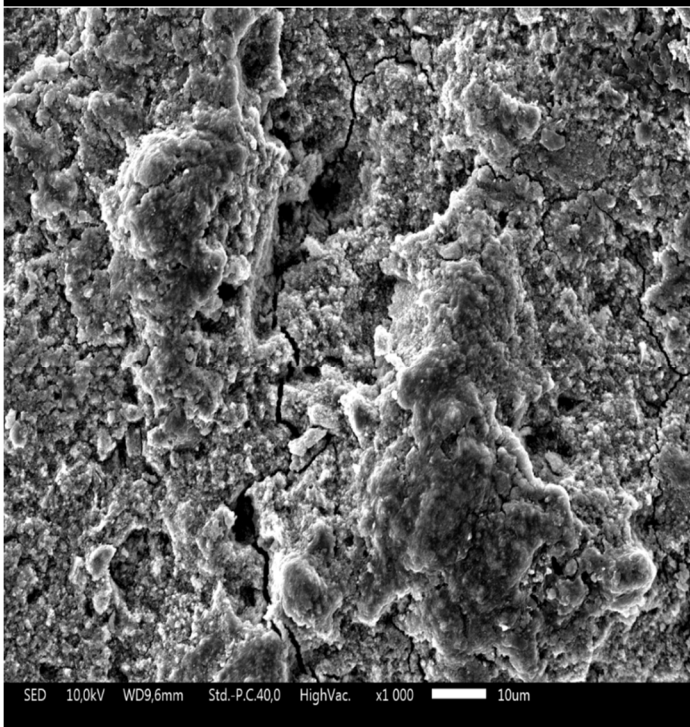
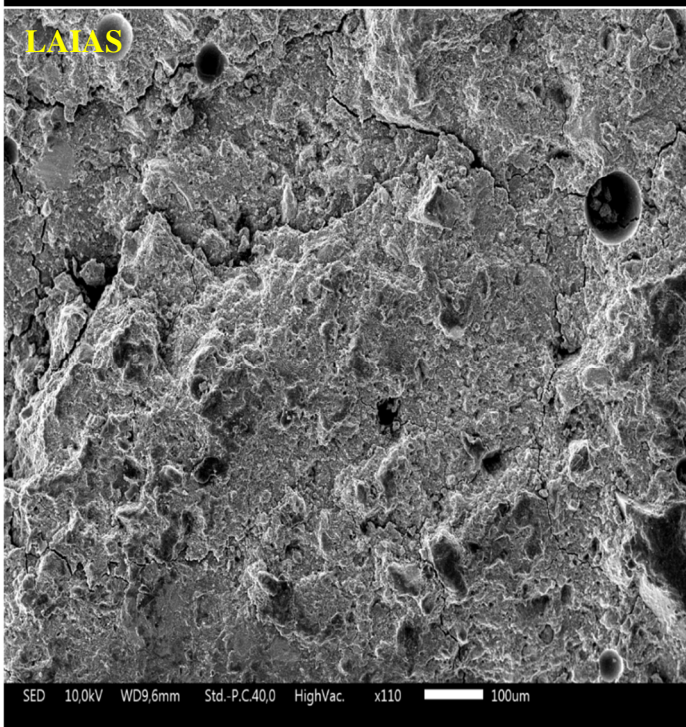
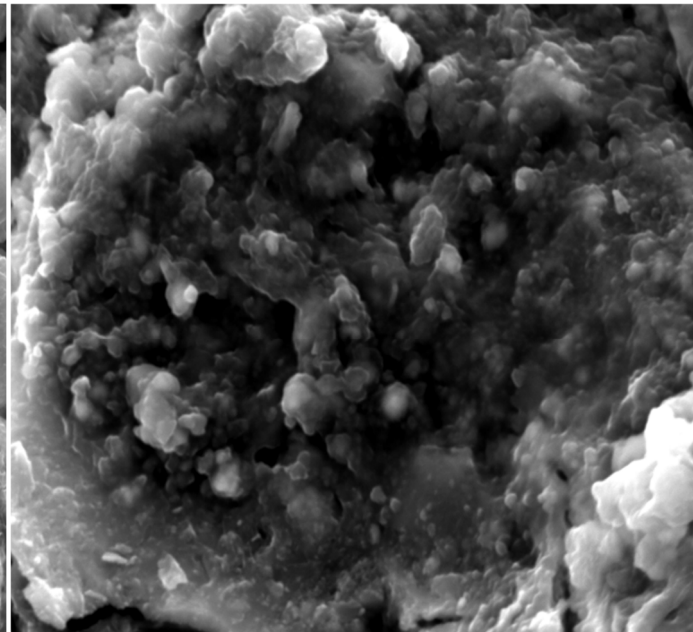
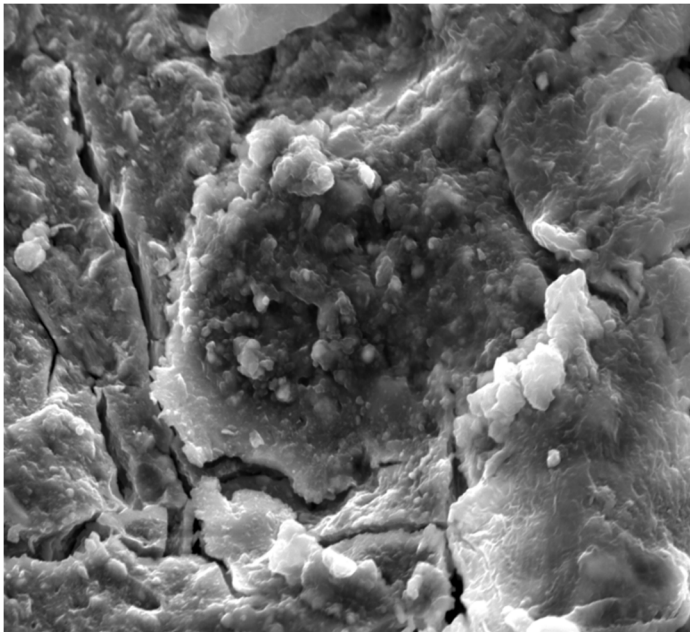
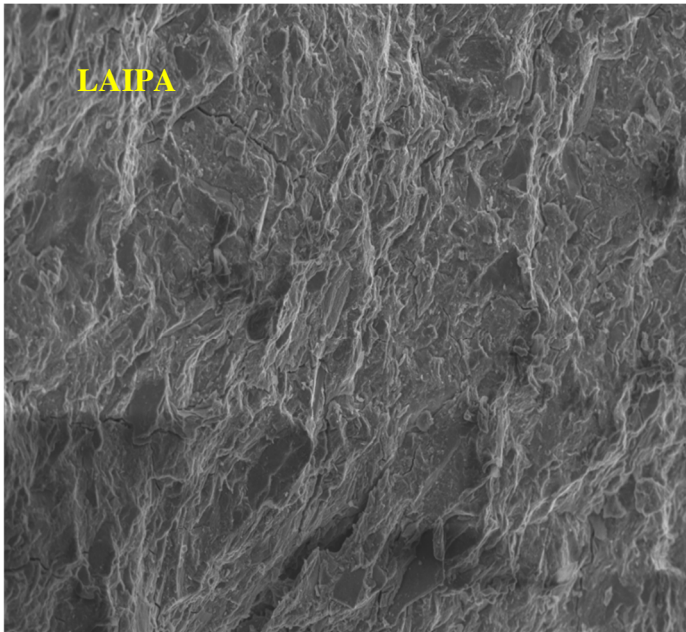


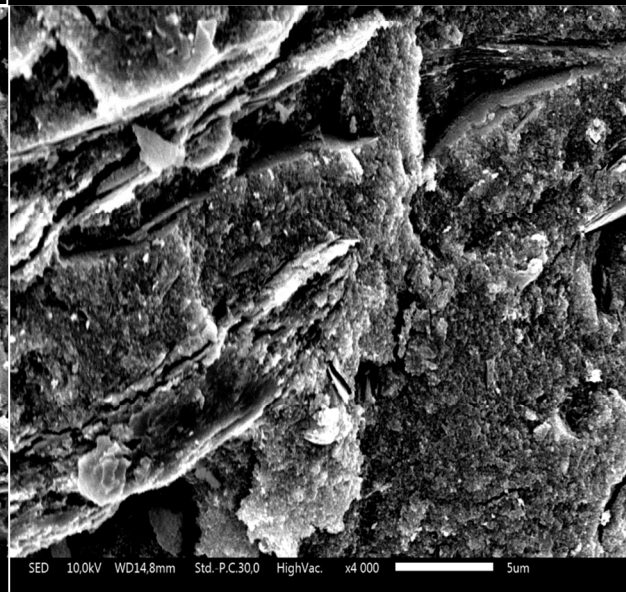
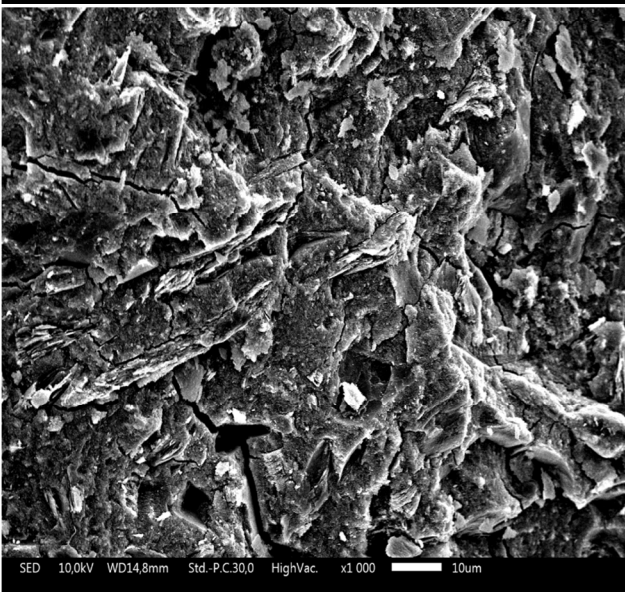
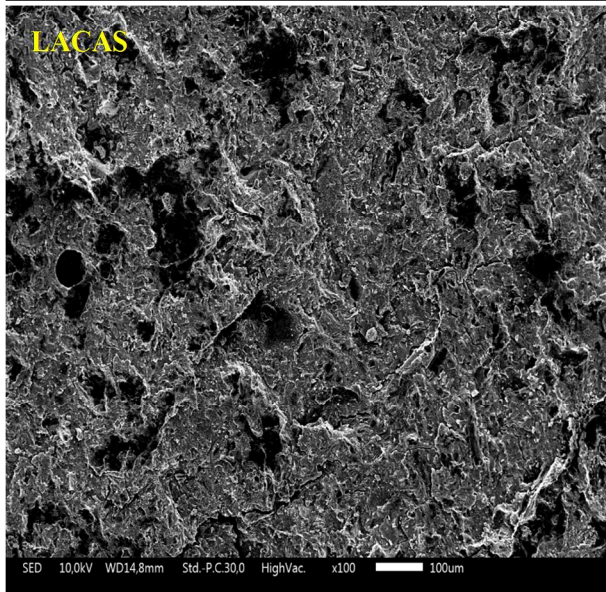
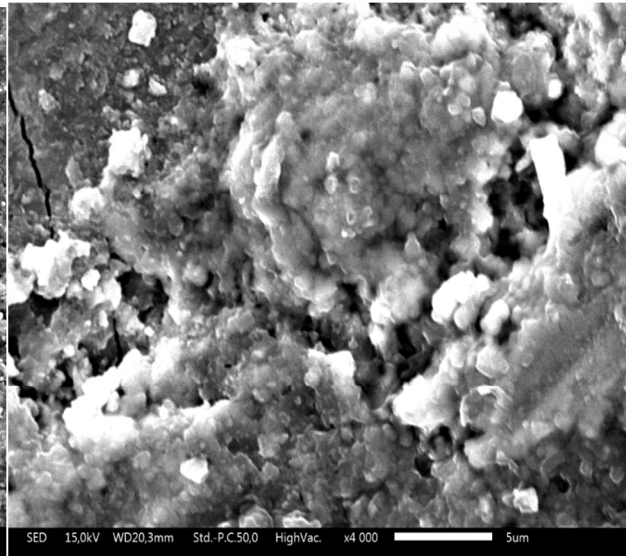
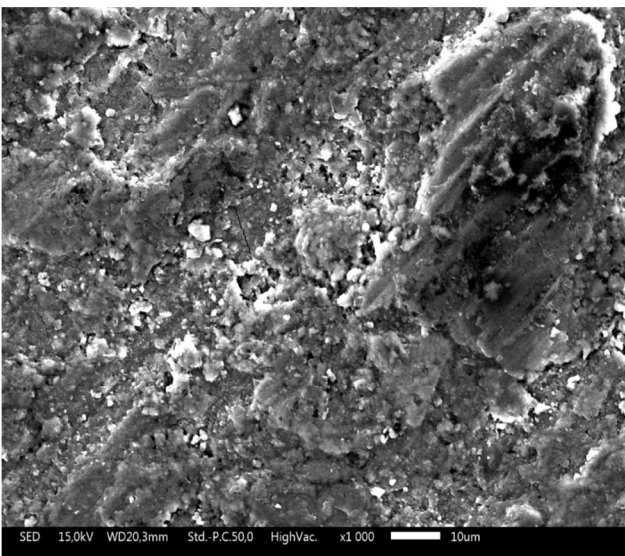
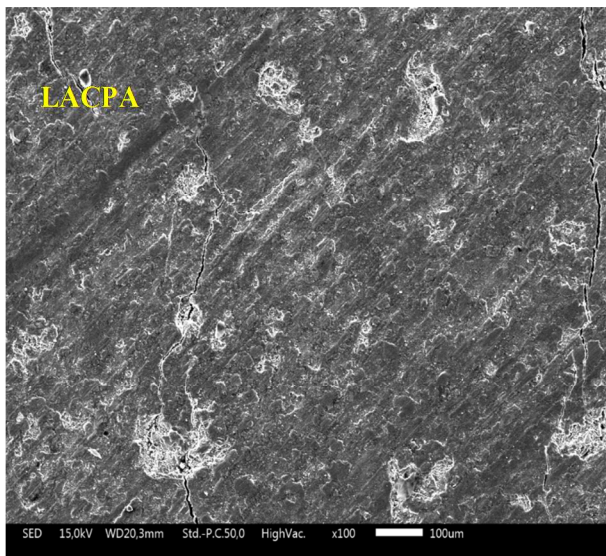


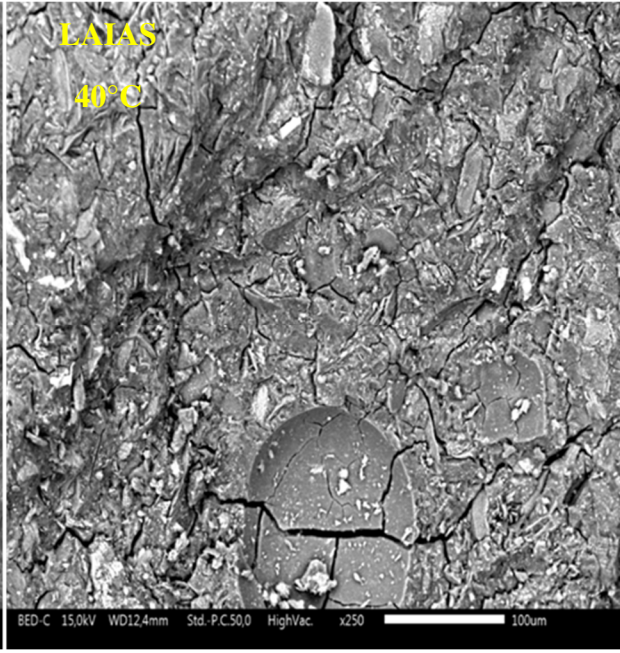
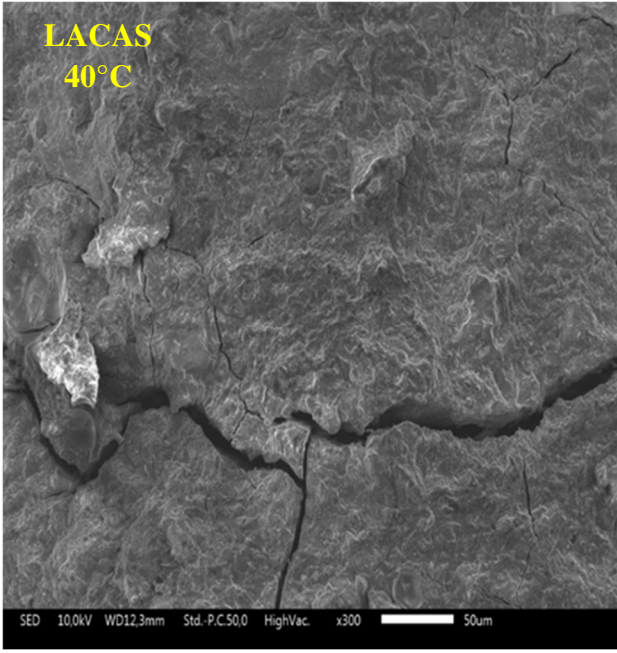


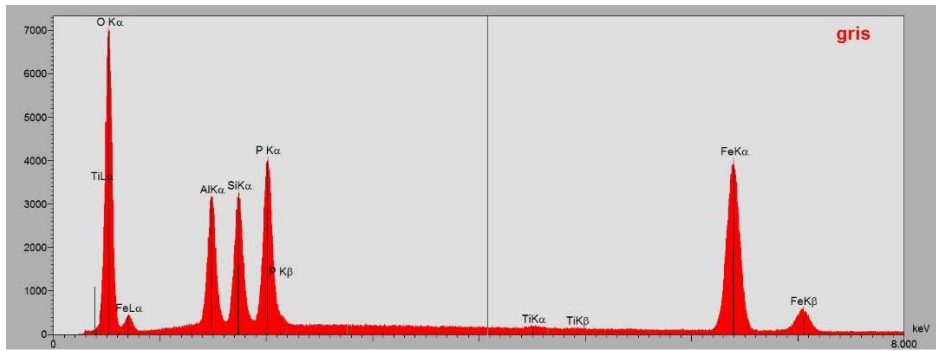
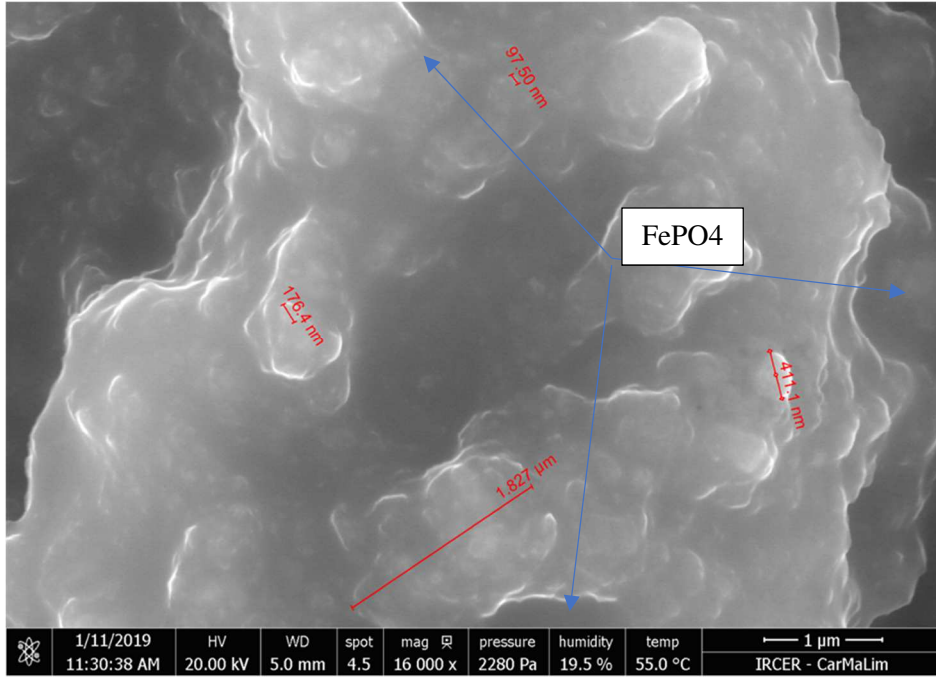


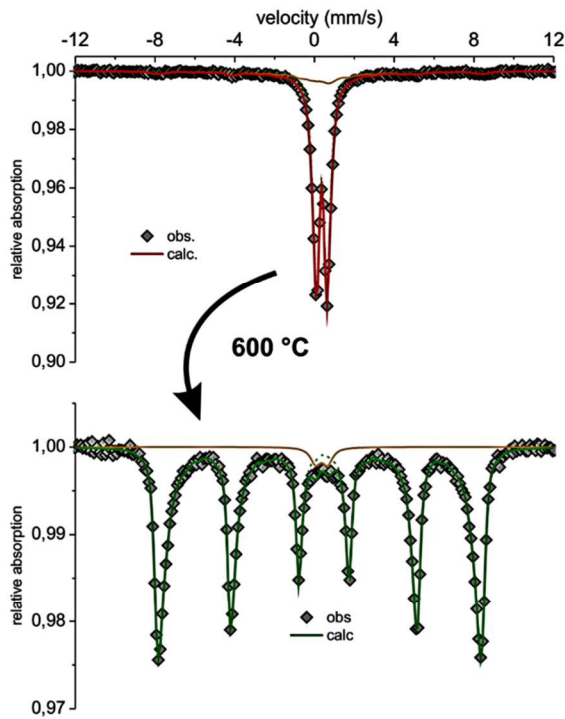




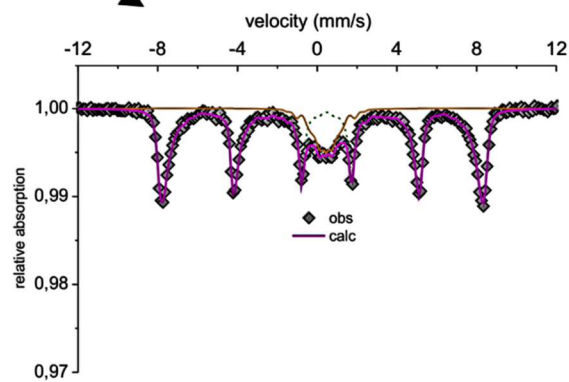
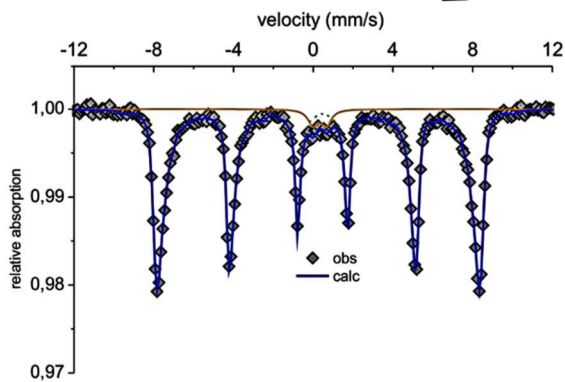


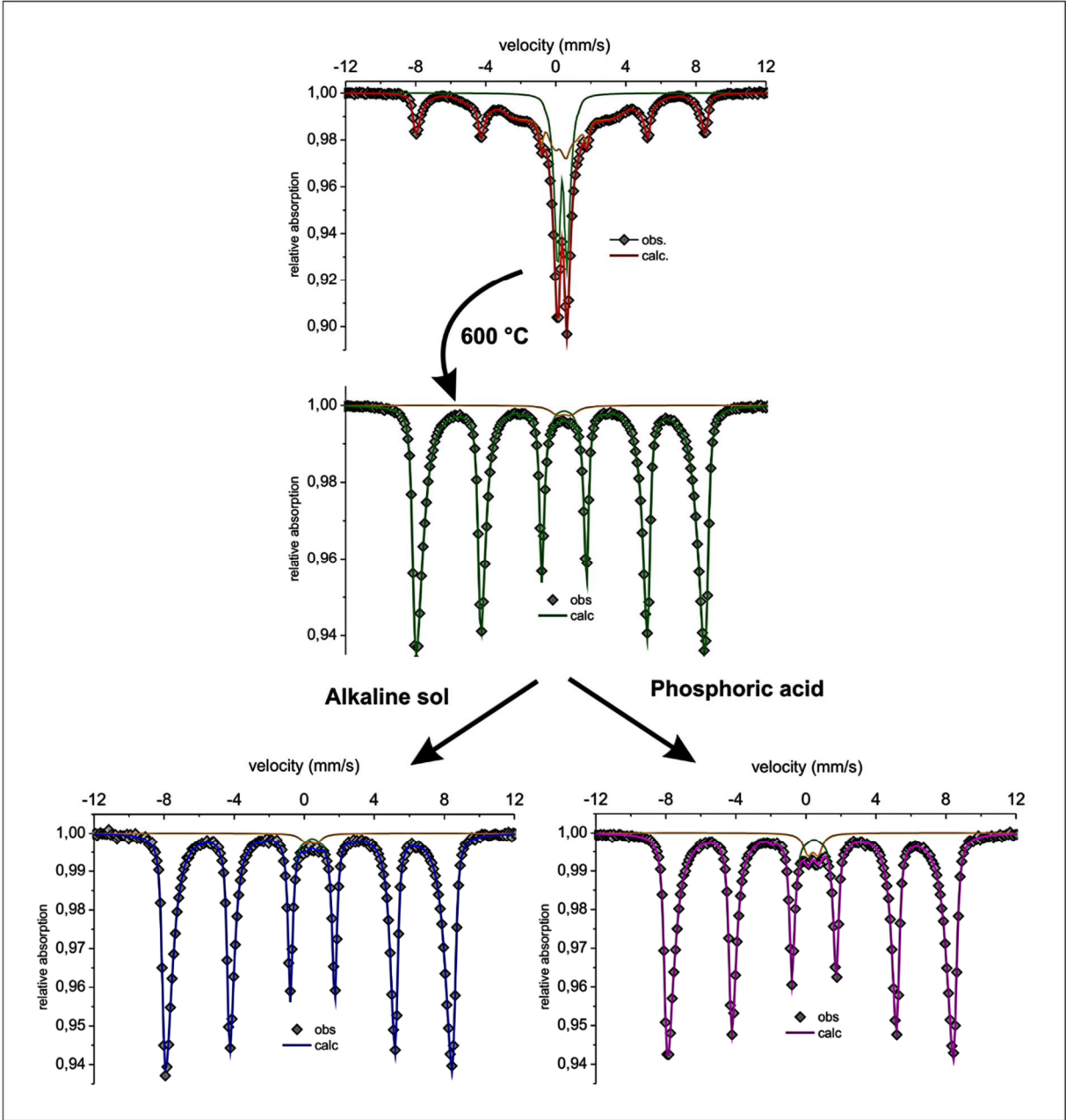






Alkaline sol Phosphoric acid





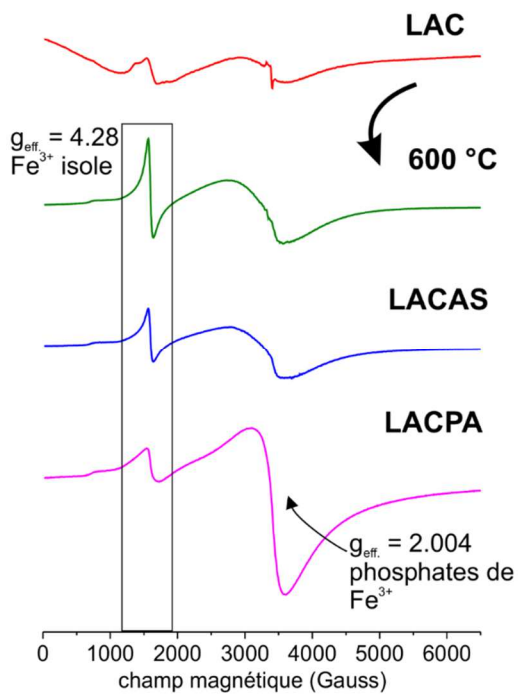
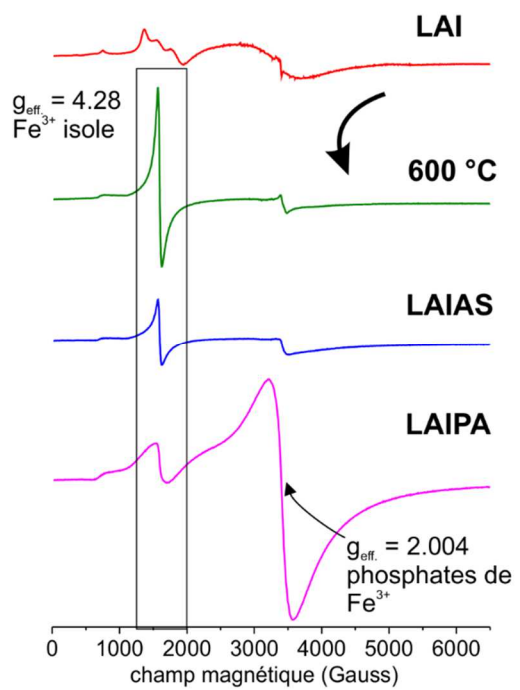


Table 1. Chemical composition of raw and calcined laterites.

| Oxides (wt.%) | Lateritic clay (LAC) | Calcined lateritic clay (LAC600) | Iron-rich laterite (LAI) | Calcined iron-rich laterite (LAI600) |
|------------------------------------|-----------------------------|---|---------------------------------|---|
| Fe₂O₃ | 13.15 | 13.07 | 49.34 | 48.93 |
| SiO₂ | 43.00 | 48.36 | 20.11 | 22.00 |
| Al₂O₃ | 28.10 | 32.35 | 17.35 | 24.40 |
| P₂O₅ | 0.23 | 0.18 | 0.33 | 0.34 |
| K₂O | 0.10 | 0.06 | 0.03 | 0.06 |
| CaO | 0.03 | 0.05 | 0.03 | 0.05 |
| TiO₂ | 2.03 | 2.51 | 0.903 | 1.12 |
| Cr₂O₃ | 0.06 | 0.07 | 0.21 | 0.18 |
| ZrO₂ | 0.05 | 0.05 | 0.03 | 0.05 |
| L.O.I | 13.33 | 3.33 | 11.66 | 3.22 |

Table 2. Compressive strength of laterite-based inorganic polymer binders cured at 20 and 40°C using alkaline solution (AS) and Phosphoric acid (PA).

| | | Compressive strength (MPa) | | | |
|-----|----|----------------------------|---------------|------------------------|-------------------------------|
| | | Curing temperature (°C) | Curing (days) | Alkaline solution (AS) | Phosphoric acid solution (PA) |
| LAI | 20 | 7 | 6 ± 1 | 39 ± 1 | |
| | | 28 | 17 ± 1 | 62 ± 1 | |
| | 40 | 7 | 15 ± 1 | 59 ± 1 | |
| | | 28 | 10 ± 1 | 65 ± 1 | |
| LAC | 20 | 7 | 29 ± 1 | 15 ± 1 | |
| | | 28 | 40 ± 1 | 38 ± 1 | |
| | 40 | 7 | 38 ± 1 | 48 ± 1 | |
| | | 28 | 30 ± 1 | 52 ± 1 | |

Table 3. Open porosity, water absorption, apparent density and thermal conductivity of laterite-based geomaterials cured at 20 and 40°C using alkaline solution (AS) and Phosphoric acid (PA).

| Samples | Open Porosity (%) at 28 days | Apparent density (g.cm ⁻³) at 28 days | Water absorption (%) at 28 days | Thermal conductivity (W.m ⁻¹ .K ⁻¹) at 7 days | Thermal conductivity (W.m ⁻¹ .K ⁻¹) at 28 days |
|---------|------------------------------|---|---------------------------------|--|---|
| LAIPA20 | 6.06 | 2.64 | 2.44 | 0.74 | 0.89 |
| LAIPA40 | 6.20 | 2.55 | 2.60 | 0.91 | 0.98 |
| LAIAS20 | 34.05 | 2.74 | 18.82 | 0.72 | 0.85 |
| LAIAS40 | 35.64 | 2.77 | 19.90 | 0.63 | 0.77 |
| LACAS20 | 41.64 | 2.31 | 30.90 | 0.62 | 0.74 |
| LACAS40 | 43.60 | 2.32 | 33.30 | 0.62 | 0.56 |
| LACPA20 | 2.97 | 2.02 | 1.51 | 0.53 | 0.78 |
| LACPA40 | 2.04 | 2.20 | 0.96 | 0.65 | 0.62 |

Table 4. Hyperfine parameters obtained from fitting of Mössbauer spectra of LAC, LAC600, LACAS and LACPA samples

| | δ (mm/s) | Δ^* (mm/s) | Γ (mm/s) | ε (mm/s) | B_{hf}^* (T) | Area (%) | Assignment |
|---------------|--------------------|----------------------|--------------------|-------------------------|-------------------|-------------|------------------------------------|
| LAC | | | | | | | |
| Dis (1) | 0.36 | - | 0.25 | -0.10 | 31 | 12 | Fe ³⁺ (Oh) Sextuplet |
| Dis (2) | 0.36 | 0.70 | 0.25 | - | - | 88 | Fe ³⁺ (Oh) DQ |
| LAC600 | | | | | | | |
| Dis (1) | 0.37 | - | 0.25 | -0.11 | 46 | 97 | Fe ³⁺ (Oh) Sextuplet |
| Site (2) | 0.36 | 0.60 | 0.60 | - | - | 3 | Fe ³⁺ (Oh) DQ |
| LACAS | | | | | | | |
| Dis (1) | 0.37 | - | 0.25 | -0.11 | 47 | 96 | Fe ³⁺ (Oh) Sextuplet |
| Site (2) | 0.32 | 0.66 | 0.60 | - | - | 4 | Fe ³⁺ (Oh) DQ |
| LACPA | | | | | | | |
| Dis (1) | 0.36 | - | 0.25 | -0.11 | 45 | 84 | Fe ³⁺ (Oh) Sextuplet |
| Dis (2) | 0.45 | 1.20 | 0.25 | - | - | 13 | Fe ³⁺ (Oh) DQ |
| Site (3) | 0.36 | 0.61 | 0.44 | - | - | 3 | Fe ³⁺ (Oh) DQ |

δ = Isomer shift

Δ^* = Quadrupole splitting distribution

Γ = Stripe width at mi-height

ε = Quadrupole shift

B_{hf}^* = Hyperfine field distribution

Table 5. Hyperfine parameters obtained from fitting of Mössbauer spectra of Mössbauer spectra of LAI, LAI600, LAIAS and LAIPA samples

| | δ (mm/s) | Δ^* (mm/s) | Γ (mm/s) | ε (mm/s) | B_{hf}^* (T) | Area (%) | Assignment |
|---------------|--------------------|----------------------|--------------------|-------------------------|-------------------|-------------|------------------------------------|
| LAI | | | | | | | |
| Dis (1) | 0.36 | - | 0.25 | -0.10 | 51 | 51 | Fe ³⁺ (Oh) Sextuplet |
| Dis (2) | 0.37 | 0.90 | 0.25 | - | - | 49 | Fe ³⁺ (Oh) DQ |
| LAI600 | | | | | | | |
| Dis (1) | 0.37 | - | 0.25 | -0.11 | 48 | 99 | Fe ³⁺ (Oh) Sextuplet |
| Dis (2) | 0.36 | 0.60 | 0.45 | - | - | 1 | Fe ³⁺ (Oh) DQ |
| LAIAS | | | | | | | |
| Dis (1) | 0.37 | - | 0.25 | -0.10 | 48 | 98 | Fe ³⁺ (Oh) Sextuplet |
| Dis (2) | 0.36 | 0.60 | 0.70 | - | - | 2 | Fe ³⁺ (Oh) DQ |
| LAIPA | | | | | | | |
| Dis (1) | 0.36 | - | 0.25 | -0.10 | 48 | 94 | Fe ³⁺ (Oh) Sextuplet |
| Dis (2) | 0.47 | 0.61 | 0.25 | - | - | 4 | Fe ³⁺ (Oh) DQ |
| Site (3) | 0.35 | 0.67 | 0.25 | - | - | 2 | Fe ³⁺ (Oh) DQ |

δ = Isomer shift

Δ^* = Quadrupole splitting distribution

Γ = Stripe width at mi-height

ε = Quadrupole shift

B_{hf}^* = Hyperfine field distribution